

# **Modulation of Tropical Instability Wave Intensity by Equatorial Kelvin Waves**

*Journal of Physical Oceanography*, 2016, 46 (9), 2623-2643

R. Holmes and L. Thomas

© Copyright [01 Sep 2016] American Meteorological Society (AMS). For permission to reuse any portion of this work, please contact [permissions@ametsoc.org](mailto:permissions@ametsoc.org). Any use of material in this work that is determined to be “fair use” under Section 107 of the U.S. Copyright Act (17 U.S. Code §?107) or that satisfies the conditions specified in Section 108 of the U.S. Copyright Act (17 USC § 108) does not require the AMS’s permission. Republication, systematic reproduction, posting in electronic form, such as on a website or in a searchable database, or other uses of this material, except as exempted by the above statement, requires written permission or a license from the AMS. All AMS journals and monograph publications are registered with the Copyright Clearance Center (<https://www.copyright.com>). Additional details are provided in the AMS Copyright Policy statement, available on the AMS website (<https://www.ametsoc.org/PUBSCopyrightPolicy>).

## Modulation of Tropical Instability Wave Intensity by Equatorial Kelvin Waves

R. M. HOLMES<sup>a</sup> AND L. N. THOMAS

*Earth System Science, Stanford University, Stanford, California*

(Manuscript received 16 March 2016, in final form 3 June 2016)

### ABSTRACT

Tropical instability waves (TIWs) and equatorial Kelvin waves are dominant sources of intraseasonal variability in the equatorial Pacific Ocean, and both play important roles in the heat and momentum budgets of the large-scale flow. While individually they have been well studied, little is known about how these two features interact, although satellite observations suggest that TIW propagation speed and amplitude are modulated by Kelvin waves. Here, the influence of Kelvin waves on TIW kinetic energy (TIWKE) is examined using an ensemble set of  $1/4^\circ$  ocean model simulations of the equatorial Pacific Ocean. The results suggest that TIWKE can be significantly modified by 60-day Kelvin waves. To leading order, TIWs derive kinetic energy from the meridional shear and available potential energy of the background zonal currents, while losing TIWKE to friction and the radiation of waves. The passage of Kelvin waves disrupts this balance. Downwelling (upwelling) Kelvin waves induce decay (growth) in TIWKE through modifications to the background currents and the TIWs' Reynolds stresses. These modulations in TIWKE affect eddy heat fluxes and the downward radiation of waves, with implications for the variability of SST and the energetics of abyssal flows in the eastern equatorial Pacific.

### 1. Introduction

Equatorial Kelvin waves in the Pacific Ocean play an important role in the El Niño–Southern Oscillation (ENSO) as they facilitate the adjustment of the upper ocean to perturbations in atmospheric forcing across the basin (Picaut et al. 1997; Suarez and Schopf 1988; Wang and Fiedler 2006). Kelvin waves are typically generated in the western Pacific by wind stress anomalies associated with tropical cyclones, the Madden–Julian oscillation, and other sources of atmospheric variability (Hendon et al. 1998; Zhang 2001). The dominant, intraseasonal, first baroclinic mode Kelvin waves propagate eastward with typical speeds of  $2.7 \text{ m s}^{-1}$  (Cravatte et al. 2003), although their propagation and structure are also influenced by the state of the background equatorial circulation (McPhaden et al. 1986;

Giese and Harrison 1990; Johnson and McPhaden 1993a,b). The Kelvin waves modify the background circulation in the central and eastern Pacific, including the thermocline depth, zonal currents, sea surface temperature (SST), and thus the air–sea interactions critical for ENSO (McPhaden and Taft 1988; Lien et al. 1995; Bergman et al. 2001; McPhaden 2002). However, the influence of Kelvin waves on smaller-scale variability in the eastern Pacific is not as well studied.

Tropical instability waves (TIWs) are a second major source of intraseasonal variability in the eastern Pacific that were first observed as meridional oscillations in the equatorial fronts (Legeckis 1977; Malardé et al. 1987; Willett et al. 2006; Jiang et al. 2009). Generated through barotropic and baroclinic instability, they travel westward with wavelengths of 700–1600 km and periods of 15–40 days (Philander 1976; Cox 1980; Qiao and Weisberg 1995; Masina et al. 1999; Kennan and Flament 2000; Lyman et al. 2007). Their strength varies both interannually with the ENSO cycle (An 2008) and seasonally, where they obtain peak amplitude in boreal fall and winter (Contreras 2002), the same period over which Kelvin wave variability peaks (Kessler et al. 1995). TIWs drive strong lateral eddy stirring and influence small-scale turbulent mixing and thus play an important role in the mixed layer heat budget (Menkes et al. 2006; Jochum

<sup>a</sup> Current affiliation: ARC Centre of Excellence for Climate System Science, Climate Change Research Centre, and School of Mathematics and Statistics, University of New South Wales, Sydney, New South Wales, Australia.

Corresponding author address: R. M. Holmes, Climate Change Research Centre, Level 4, Matthews Building, University of New South Wales, Sydney, NSW 2052, Australia.  
E-mail: ryan.holmes@unsw.edu.au

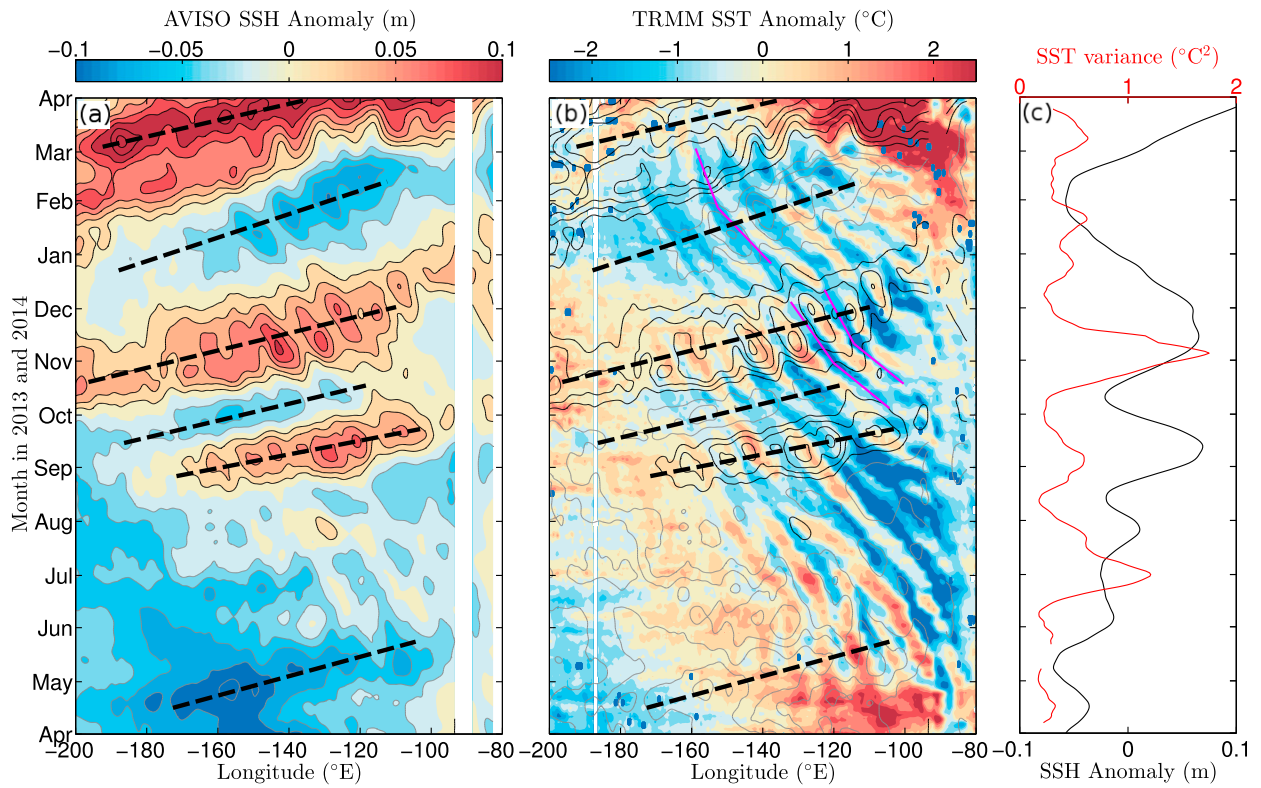


FIG. 1. (a) SSH anomalies from AVISO altimetry data averaged between  $\pm 2^{\circ}$  latitude in 2013 and 2014. Raw SSH anomalies are filtered with a  $3.75^{\circ}$  moving average in longitude and 15-day moving average in time. (b) TMI TRMM microwave satellite SST anomalies (Wentz et al. 2015) averaged between  $1^{\circ}$  and  $2^{\circ}\text{N}$ . The 3-day average SST anomalies are filtered with a  $0.75^{\circ}$  moving average in longitude and 3-day moving average in time. Downwelling and upwelling Kelvin wave phases are marked with black dashed lines. Black (gray) contours show positive (negative) perturbation SSH in both (a) and (b). Several TIW phases are marked with magenta lines in (b). (c) SST variance (red) and SSH anomalies from (a) and (b) averaged between  $-140^{\circ}$  and  $-120^{\circ}\text{E}$ .

et al. 2007; Moum et al. 2009; Graham 2014; Holmes and Thomas 2015).

Several studies have highlighted the potential for interactions between TIWs and Kelvin waves. Harrison and Giese (1988) and Giese and Harrison (1991) saw modulations in TIW amplitude in a numerical model in response to the presence of Kelvin waves and inferred changes in the TIW-driven meridional heat flux. In the observations of Qiao and Weisberg (1998), the end of the TIW season coincided with the arrival of a strong intraseasonal Kelvin wave from the western Pacific, which they suggest may have decreased the meridional shear in the background zonal currents, resulting in a decay in TIW amplitude. Finally, a number of studies have discussed the potential link between the intra-seasonal wind variability that generates Kelvin waves, Rossby waves reflected from the eastern boundary, and the strength and phasing of TIWs (Allen et al. 1995; Lawrence et al. 1998; Lawrence and Angell 2000; Benestad et al. 2001). All of these studies hint at the potential importance of interactions between free

equatorial waves and TIWs for setting the magnitude and temporal evolution of SST anomalies in the eastern equatorial Pacific in response to variations in atmospheric forcing. However, no study has yet explored the details of how Kelvin waves influence the TIW kinetic energy (TIWKE) budget.

Analysis of satellite sea surface height (SSH) and SST data in the equatorial Pacific suggests that Kelvin waves may alter both the phase speed and amplitude of TIWs (Fig. 1). In late 2013 and early 2014, several downwelling (positive SSH anomaly) and upwelling (negative SSH anomaly) Kelvin waves propagated across the Pacific (Fig. 1a), encountering an energetic set of westward-propagating TIWs (Fig. 1b). The TIWs appear to propagate faster during the upwelling phases and slower during the downwelling phases (magenta phase lines in Fig. 1b), as might be expected from Doppler shifting associated with the Kelvin wave zonal velocity. In addition, the strength of the SST anomalies associated with the TIWs, a proxy for the TIW amplitude, appears to vary with the Kelvin wave phase. Stronger SST anomalies

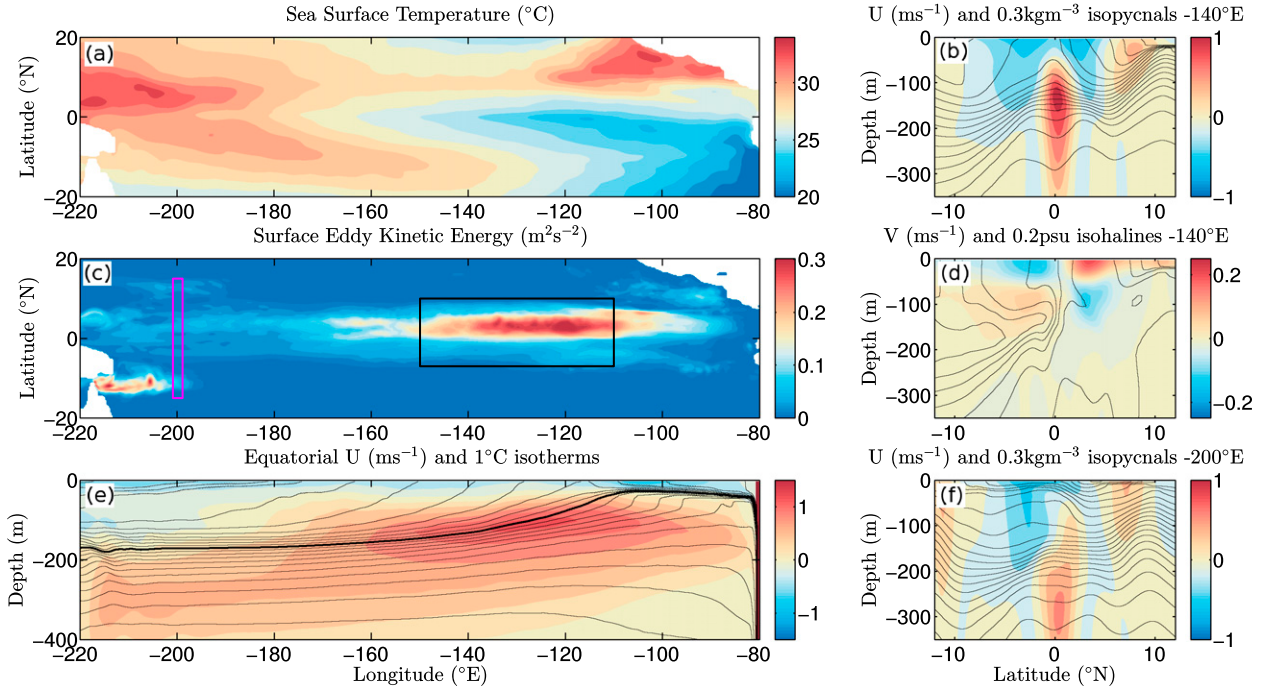


FIG. 2. (a) SST and (c) surface eddy kinetic energy taken from the control simulation. Meridional sections of (b) zonal velocity and density and (d) meridional velocity and salinity at  $-140^{\circ}\text{E}$ . (e) Zonal section of zonal velocity and temperature at the equator. The thick contour is the  $21^{\circ}\text{C}$  isotherm. (f) Meridional section of zonal velocity and density at  $-200^{\circ}\text{E}$ . The black box in (c) indicates the control volume used for the TIWKE budget, and the magenta box indicates the Kelvin wave forcing region. The contour interval is indicated at the top of (b),(d),(e), and (f).

occur following upwelling phases and weaker anomalies occur after downwelling phases (e.g., October–December 2013 between  $-140^{\circ}$  and  $-110^{\circ}\text{E}$  in Fig. 1).

Motivated by these observations and previous studies, we address the following question: How do intraseasonal Kelvin waves influence the properties of TIWs in the equatorial Pacific? To answer this question, we use a set of  $1/4^{\circ}$  ocean model simulations of the equatorial Pacific forced with first baroclinic mode Kelvin waves in the western Pacific and analyze the energetics of the TIWs with and without Kelvin waves.

## 2. Ocean model setup

We will examine the interaction between equatorial Kelvin waves and TIWs in a set of Regional Ocean Modeling System (ROMS; Shchepetkin and McWilliams 2005) simulations. The simulations span the Pacific Ocean over the region  $30^{\circ}\text{S}$  to  $30^{\circ}\text{N}$ ,  $-240^{\circ}$  to  $-70^{\circ}\text{E}$  with  $1/4^{\circ}$  horizontal resolution, 50 vertical levels, and a time step of 10 min. They are spun up from rest over a 10-yr period using initial conditions, forcing, and boundary conditions taken from the Common Ocean Reference Experiment Normal Year Forcing (CORENYF) fields (Large and Yeager 2004). Analysis shown here is from the final year of the spinup period (hereinafter the

“control simulation”). The K-profile parameterization was used to parameterize subgrid-scale vertical mixing processes (Large et al. 1994). Horizontal diffusion of momentum was achieved with a biharmonic viscosity with coefficient  $1 \times 10^{11} \text{ m}^4 \text{ s}^{-1}$  and harmonic horizontal diffusion of salinity and temperature was included with coefficient  $100 \text{ m}^2 \text{ s}^{-1}$ . ROMS has been successfully used for process studies of TIWs under similar configurations (Marchesiello et al. 2011; Holmes et al. 2014; Holmes and Thomas 2015).

To simplify the analysis and interpretation, we remove the seasonal cycle by using temporally constant atmospheric forcing. Surface forcing, initial conditions, and boundary conditions are taken from 6-month July–December averages of the CORENYF bulk forcing fields. This season has strong trade winds and produces energetic TIWs, ideal for this process study.

The simulations produce a general circulation with similar features to observations (Fig. 2). A sloped thermocline leans upward toward the eastern Pacific cold tongue that is bounded by warmer water to the north (Figs. 2a,e). The SSTs are warmer than observed in the far western Pacific and in the Costa Rica dome region, as there is no wind stress variability (Fig. 2a). The cold tongue SST is  $1^{\circ}$ – $2^{\circ}\text{C}$  cooler than observed annual-mean values, and the Equatorial Undercurrent (EUC) is

slightly stronger than annual-mean observations, reaching  $1.1 \text{ m s}^{-1}$  (Fig. 2b). The simulations produce a statistically steady TIW field with surface eddy kinetic energy (EKE) exceeding  $0.2 \text{ m}^2 \text{s}^{-2}$  (comparable to peak observed EKE values; Flament et al. 1996) over an extensive area reaching from  $-150^\circ$  to  $-100^\circ\text{E}$  (Fig. 2c). The TIWs have a dominant period near 34 days (not shown).

### 3. TIW energetics in the control simulation

In this section, we examine the TIWKE budget in the statistically steady control simulation that does not contain Kelvin waves. The ocean model solves the hydrostatic primitive equations, which can be written in terms of buoyancy as

$$\frac{D\mathbf{u}_h}{Dt} + f\hat{\mathbf{k}} \times \mathbf{u} = -\frac{1}{\rho_0} \nabla_h P + \mathbf{F}_h, \quad (1)$$

$$0 = -\frac{1}{\rho_0} \frac{\partial P}{\partial z} + b, \quad (2)$$

$$\nabla \cdot \mathbf{u} = 0, \text{ and} \quad (3)$$

$$\frac{Db}{Dt} = \mathcal{D}, \quad (4)$$

where  $\mathbf{u} = (u, v, w)$  is the three-dimensional velocity,  $\mathbf{u}_h$  is the horizontal velocity,  $f = 2\Omega \sin\theta$  is the Coriolis parameter,  $\Omega$  is the rotation rate of Earth,  $\theta$  is latitude,  $\hat{\mathbf{k}}$  is the unit vector in the local vertical,  $\rho_0$  is a reference density,  $P$  is the pressure,  $\mathbf{F} = (F_x, F_y, 0)$  is the frictional force,  $b = -g\rho/\rho_0$  is the buoyancy,  $\rho$  is the potential density,  $g$  is the acceleration due to gravity, and  $\mathcal{D}$  represents diabatic processes. We now perform a Reynolds decomposition of the flow field into background and eddy or TIW components:  $\mathbf{u} = \bar{\mathbf{u}} + \mathbf{u}' = \mathbf{U} + \mathbf{u}'$ . In the control simulation, the overbar denotes a time average over the whole year and the time-varying flow components are the TIWs. For the Kelvin wave simulations considered in the next section, the overbar will denote an ensemble average, and both background and TIW flow components will vary in time.

Using the standard procedure (see, e.g., Masina et al. 1999), an equation for the evolution of eddy KE or TIWKE,

$$\mathcal{K} = 0.5\rho_0(\overline{u'u'} + \overline{v'v'}), \quad (5)$$

can be derived from the equations of motion (1)–(4):

$$\begin{aligned} \frac{\partial \mathcal{K}}{\partial t} = & -\nabla \cdot [\mathcal{K}\mathbf{U} + \overline{\mathbf{u}'P'} + 0.5\rho_0\overline{\mathbf{u}'(u'u' + v'v')} ] + \rho_0\overline{w'b'} \\ & + \rho_0\overline{\mathbf{u}' \cdot \mathbf{F}_H} - \rho_0\overline{\mathbf{u}'u'} \cdot \nabla U - \rho_0\overline{\mathbf{u}'v'} \cdot \nabla V. \end{aligned} \quad (6)$$

The time tendency term on the left-hand side is zero for the control simulation but nonzero for the ensemble simulations considered in the next section. The terms on the right-hand side are the convergence of the mean, pressure, and TIW fluxes of TIWKE, the potential energy (PE) conversion term, the frictional term, and the shear production terms of which there are six associated with each of the spatial derivatives of the background zonal  $U$  and meridional  $V$  velocities. These terms are evaluated from the daily averaged model output. The frictional and pressure flux divergence terms are calculated by taking the dot product of the velocity with the model diagnostic frictional and pressure gradient forces. Thus, we calculate the divergence of the pressure fluxes directly and not the individual flux components.

The TIWKE budget in the control simulation is dominated by production of TIWKE by lateral shear production acting on the meridional shear in the zonal velocity,

$$\text{LSP} = -\rho_0\overline{u'u'} \frac{\partial U}{\partial y} \quad (7)$$

(Figs. 3b,e), conversion of mean PE to TIWKE (Figs. 3c,f), the transport of TIWKE by pressure fluxes (Fig. 3i), and the removal by friction (Fig. 3h). Integrating the budget over a control volume bounding the TIW region spanning the top 244 m,  $7^\circ\text{S}$  to  $10^\circ\text{N}$  and  $-150^\circ$  to  $-110^\circ\text{E}$ , shows that PE conversion is the largest net source ( $17.6 \pm 1.0 \text{ GW}$ ) followed by LSP ( $12.6 \pm 1.5 \text{ GW}$ ).<sup>1</sup> The LSP has two source regions: one associated with the cyclonic shear between the EUC and the South Equatorial Current (SEC) near  $1.5^\circ\text{N}$  at 70-m depth and one associated with the anticyclonic shear between the SEC and the North Equatorial Counter-current (NECC) near the surface at  $4^\circ\text{N}$  (cf. Figs. 3b,e and 2b). There is also a sink region on the southern side of the EUC. The conversion from mean PE has a peak farther north near  $5^\circ\text{N}$  (Fig. 3f) and a source region in the Southern Hemisphere east of  $-140^\circ\text{E}$  (Fig. 3c). These TIWKE source terms are broadly consistent with the previous literature, although the exact mix of source regions and strengths varies with the season and model

<sup>1</sup>The uncertainty of these volume-integrated values was estimated by calculating the spread between 10 sets constructed by rejecting a random 10% of the 360 days in the control simulation for each set. The 10 sets were chosen for consistency with the ensemble simulations described in the next section and for computational reasons. To account for temporal autocorrelation (which is not a problem for the ensemble simulations considered in the next section) the degrees of freedom were reduced by  $34/3$  as 34 days was the TIW period, and we assume that the TIWs are perfect sinusoids that require three sampling points to constrain.

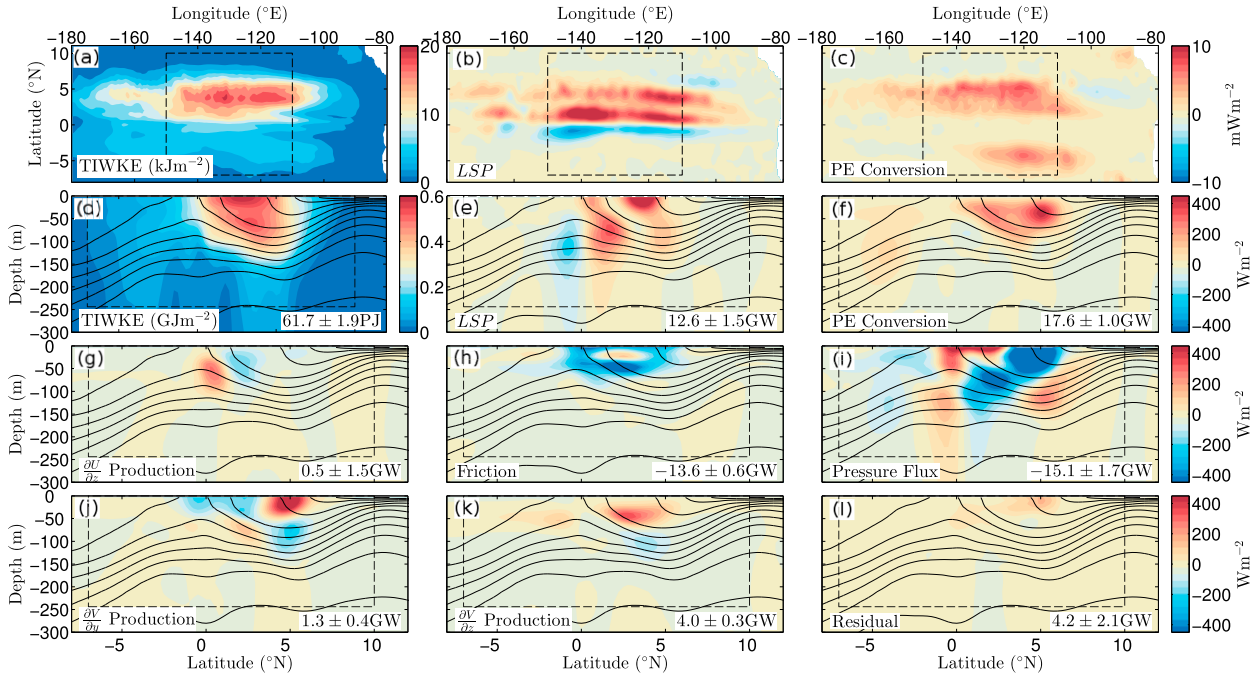


FIG. 3. Longitude–latitude plots of (a) TIWKE, (b) LSP [see Eq. (7)], and (c) conversion of mean PE into TIWKE from the control simulation integrated over the top 244 m. Latitude–depth plots of (d) TIWKE and (e)–(l) TIWKE energy budget terms [see Eq. (6)] integrated between the longitudes of  $-150^{\circ}$  and  $-110^{\circ}$ E. The dashed lines show the control volume ( $7^{\circ}$  to  $10^{\circ}$ N,  $-150^{\circ}$  to  $-110^{\circ}$ E, top 244 m) over which each term is integrated, with the totals shown in the bottom right of (d)–(l). The contours in (d)–(l) are isopycnals at  $0.5 \text{ kg m}^{-3}$  spacing. The net TIWKE budget is dominated by creation of TIWKE through LSP in (b) and (e) and PE conversion in (c) and (f), removal of TIWKE by friction in (h), and radiation of energy out of the control volume by the pressure fluxes in (i). The residual in (l) has a lower magnitude than these four main terms.

(Luther and Johnson 1990; Masina et al. 1999; Pezzi and Richards 2003). The other shear production terms make small contributions that overall are not large sources or sinks of TIWKE (Figs. 3g,j,k; note that the  $\partial V/\partial x$  production term is not shown because it is negligible).

Friction is a large sink of TIWKE in the control volume ( $-13.6 \pm 0.6$  GW; Fig. 3h), mostly in the upper EUC and SEC region where TIWs are known to drive strong variations in vertical mixing (Moum et al. 2009; Holmes and Thomas 2015). The divergence of the pressure flux suggests that energy is radiated away from the regions in which it is generated by LSP and PE conversion (cf. Fig. 3i to Figs. 3e and 3f). Some energy is deposited in surrounding regions at the surface near the equator and between 100 and 150 m at  $5^{\circ}$ N (Fig. 3i), helping to expand the spatial extent of the TIWKE (cf. Fig. 3i to Fig. 3d). However, energy radiation out of the control volume via pressure fluxes is also the largest mechanism of TIWKE loss, accounting for  $-15.1 \pm 1.7$  GW. Of this outward pressure flux,  $6.4 \pm 0.5$  GW is dissipated in the model layer near the seafloor, where the eddy KE budget is dominated by a balance between pressure flux convergence and friction due to quadratic bottom drag (not shown). Of the remaining  $8.7 \pm 2.2$  GW

leaving the control volume,  $6 \pm 0.6$  GW is lost through the lateral boundaries at all depths (as calculated by integrating the pressure flux divergence over the full water column), leaving  $2.7 \pm 2.8$  GW to be lost to friction and other processes within the deep-water column below 244 m but above the bottom model layer.

The loss of  $6 \pm 0.6$  GW of energy through lateral radiation is partially accounted for by meridionally propagating barotropic Rossby waves generated by the TIWs. These were discussed by Farrar (2011) in the context of altimetry observations. Barotropic waves are evident in the model SSH (Fig. 4a) and barotropic velocity (Fig. 4b) fields, with wave crests oriented northwest (NW)–southeast (SE) in the Northern Hemisphere and SW–NE in the Southern Hemisphere. Using estimates of the zonal wavelength (1300 km), period (34 days), and the dispersion relation for barotropic Rossby waves (see Farrar 2011),

$$\omega = \frac{-\beta k}{k^2 + l^2}, \quad (8)$$

where  $\omega$  is the frequency,  $\beta = \partial f/\partial y$ , and  $k$  and  $l$  are the zonal and meridional wavenumbers, respectively,

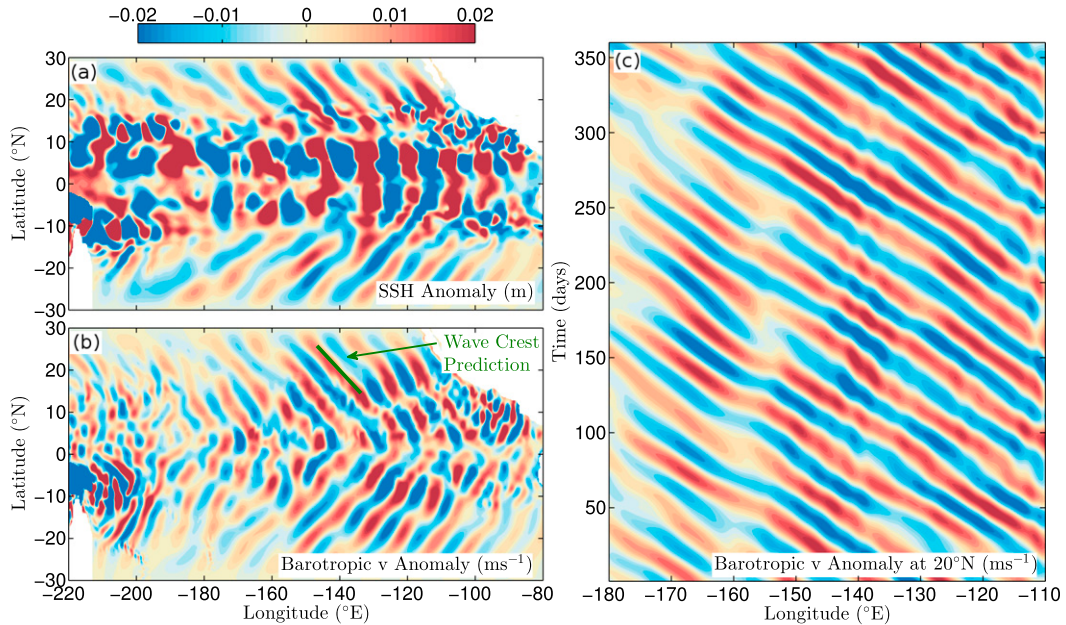


FIG. 4. (a) SSH and (b) barotropic meridional velocity  $v$  anomalies from the temporal mean on day 44 of the control simulation. (c) Longitude–time plot of the deviation barotropic meridional velocity at 20°N. The color scale in (a) is saturated to emphasize the wave signals poleward of ±12° latitude. Using estimates of the wavelength (1300 km), period (34 days), and the dispersion relation for barotropic Rossby waves [Eq. (8)] gives a good prediction for the orientation of wave crests [green line in (b)].

gives a good prediction for the orientation of wave crests at 20°N in the model (green line in Fig. 4b), suggesting that these waves are indeed barotropic Rossby waves. In addition, using estimates of the velocity anomaly amplitude  $u_a = v_a = 0.02 \text{ m s}^{-1}$  (Figs. 4b,c) and SSH anomaly amplitude  $\zeta_a = 0.02 \text{ m}$  (Fig. 4a), we can obtain an estimate of the net meridional energy flux associated with these waves  $F = L\bar{E}c_g$ , where  $L = 4400 \text{ km}$  is the zonal length of the control volume between  $-150^\circ$  and  $-110^\circ\text{E}$ , and the wave period-averaged energy density  $\bar{E}$  and meridional group velocity  $c_g$  are given by

$$\bar{E} = 0.5[0.5\rho_0H(u_a^2 + v_a^2) + 0.5\rho_0g\zeta_a^2], \quad \text{and} \quad (9)$$

$$c_g = \frac{2\beta kl}{(k^2 + l^2)^2}. \quad (10)$$

Using the above parameters, we obtain an estimated northward flux of 1.7 GW, and thus if there is an equivalent southward flux in the Southern Hemisphere, then the total flux of energy lost through barotropic Rossby wave radiation would account for over half of the  $6 \pm 0.6 \text{ GW}$  of energy lost from the TIWKE budget through lateral pressure flux radiation. Thus, barotropic Rossby wave radiation appears to play an important role in the TIWKE budget.

#### 4. Kelvin wave ensemble experiments

In this section, we describe the setup of the ensemble experiments used to study the interaction of equatorial Kelvin waves with the statistically steady TIW field. In these experiments, we nudge the model horizontal velocity in the western Pacific to force first baroclinic mode equatorial Kelvin waves with known properties. We force the Kelvin waves between the longitudes of  $-201^\circ$  and  $-199^\circ\text{E}$ , where TIWKE is minimal (magenta box in Fig. 2c). There is a nonzero background flow and meridional variations in stratification at this location (Fig. 2f), which influence the spatial structure of the Kelvin wave mode. To take this into account, we solve for the structure of a linear Kelvin wave in the control simulation background flow at this location, assuming that this background flow is zonally uniform. The eigenvalue calculation is described in the appendix and is similar to that described by McPhaden et al. (1986). The assumption of zonal uniformity is expected to work well in the forcing region in the western Pacific, where zonal variations are weak (Fig. 2e). The first baroclinic mode Kelvin wave obtained from this calculation at  $-200^\circ\text{E}$  has a wave speed of  $c = 2.80 \text{ m s}^{-1}$  and an altered spatial structure relative to an ideal Kelvin wave without a background flow (cf. Figs. 5a and 5c). In comparison, at  $-140^\circ\text{E}$  the linear first baroclinic mode Kelvin wave

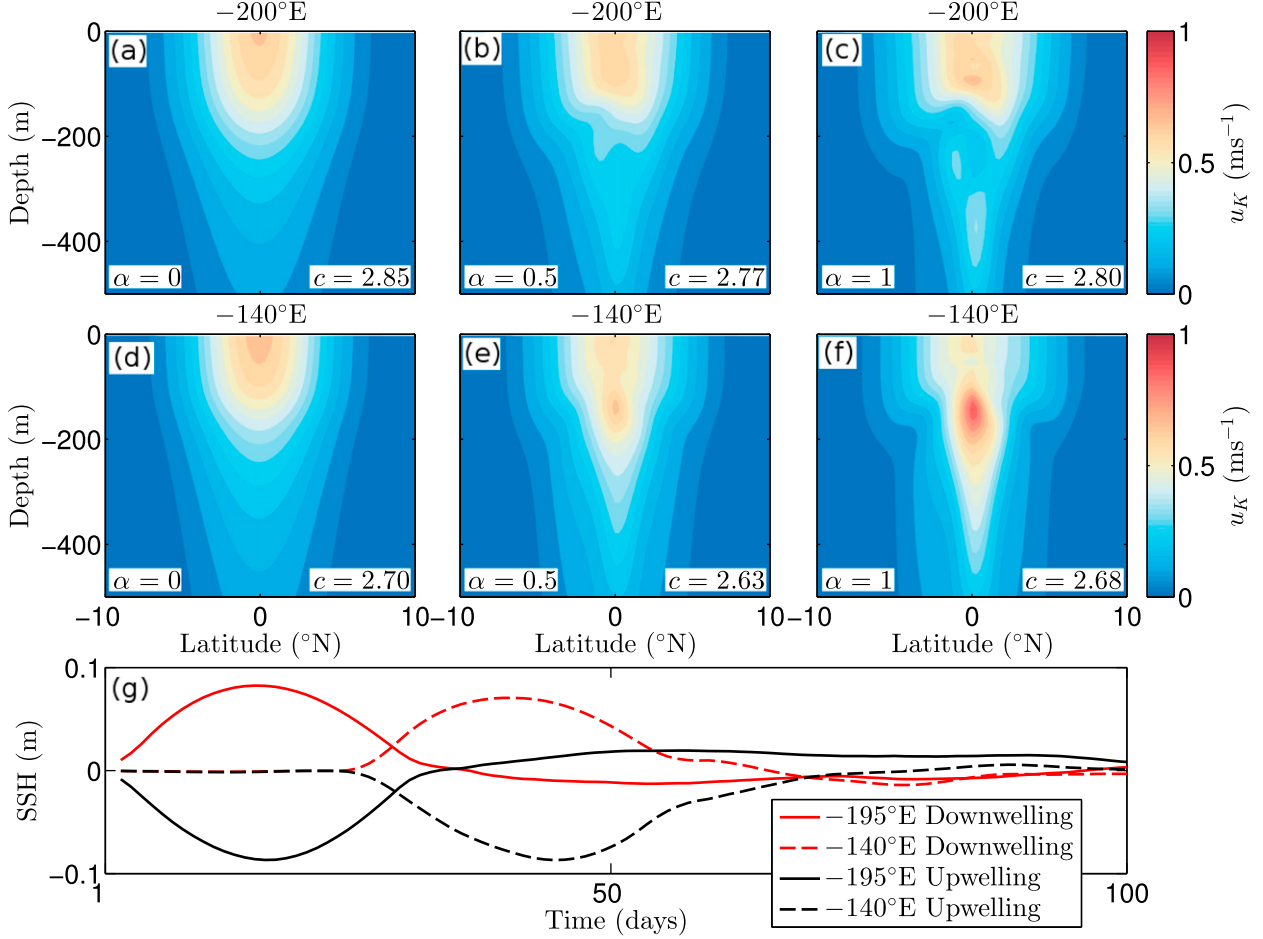


FIG. 5. (a)–(f) The zonal velocity of the first baroclinic mode Kelvin wave as a function of the mean flow strength  $\alpha$ , where  $\alpha = 0$  indicates no mean flow and  $\alpha = 1$  indicates the full mean flow [see Eq. (A14)]. For (a)–(c), the mean flow and stratification used is that at  $-200^{\circ}\text{E}$  in the western Pacific (Fig. 2f) and for (d)–(f) the mean flow used is that at  $-140^{\circ}\text{E}$  in the eastern Pacific (Fig. 2b) from the control simulation. The corresponding wave speeds ( $\text{m s}^{-1}$ ) are indicated in the subplot titles. As the mean flow is introduced [going from (a) to (c) and (d) to (f)], the mode acquires some small-scale structure, but the large-scale pattern remains the same. (g) Time series of ensemble average SSH from downwelling (red) and upwelling (black) experiments at  $-195^{\circ}$  (solid) and  $-140^{\circ}\text{E}$  (dashed).

has a stronger amplitude around the EUC core than at  $-200^{\circ}\text{E}$  (cf. Figs. 5f and 5c) because the EUC is stronger at  $-140^{\circ}\text{E}$ . The phase speed of  $2.68 \text{ m s}^{-1}$  at  $-140^{\circ}\text{E}$  is also slightly slower than that at  $-200^{\circ}\text{E}$ . These phase speeds are consistent with that measured in the equatorial Pacific (Cravatte et al. 2003). To force the Kelvin wave, the zonal flow between  $-201^{\circ}$  and  $-199^{\circ}\text{E}$  is nudged to the background flow (Fig. 2f) plus the spatial structure in Fig. 5c multiplied by a half-sine temporal factor with given frequency  $\omega$ . The temporal factor represents either a downwelling half-sine Kelvin wave pulse or an upwelling half-sine Kelvin wave pulse, which differ by a phase shift of  $\pi$  (illustrated in Fig. 5g). The nudging time scale used is  $1/3$  day.

When constructing an energy budget for the TIWs, it is necessary to separate the flow into TIW and

background flow components. For the control simulation, this was done using a simple time average. However, when introducing temporal variability in the background flow in the form of a propagating Kelvin wave with a time scale not necessarily well separated from the TIW time scale, this method no longer works. Another possibility is to use a longitude filter, but again the zonal scale of the TIWs and Kelvin waves are not necessarily well separated. To avoid these problems, we perform an ensemble of 10 simulations for both the downwelling and upwelling cases. Each ensemble member consists of a single Kelvin wave pulse forced for 30 days in the western Pacific followed by a spin-down period of 120 days (Fig. 5g). The Kelvin wave forcing is initialized from different times in the control simulation for each ensemble member and thus the

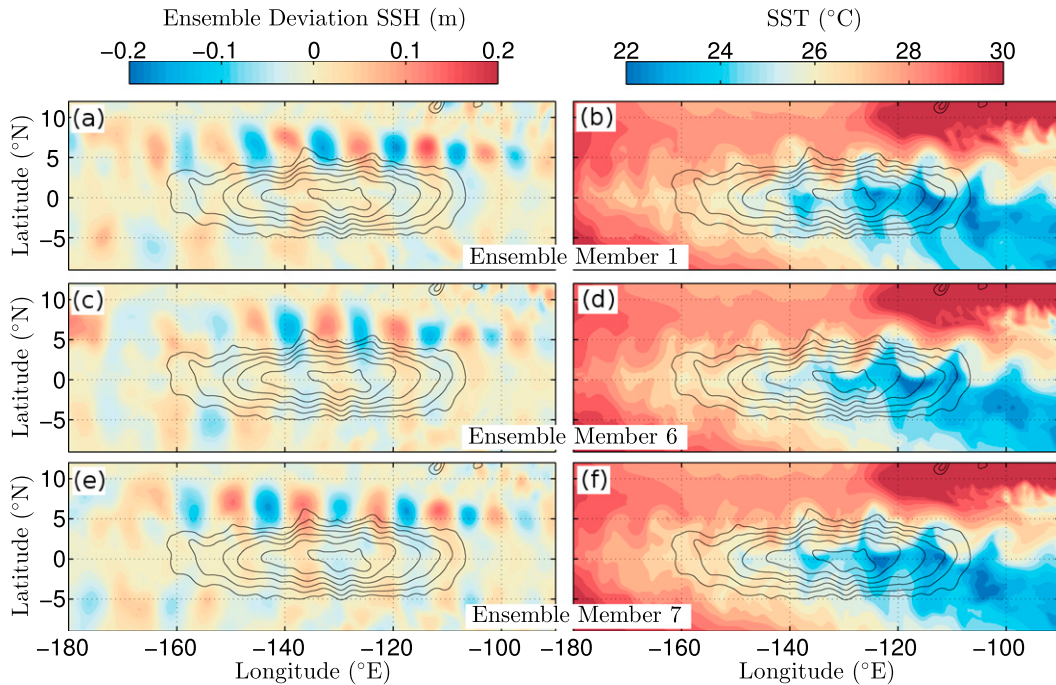


FIG. 6. (a),(c),(e) SSH deviation from the ensemble mean and (b),(d),(f) SST for three ensemble members of the downwelling Kelvin wave experiment at day 45; 0.01-m contours of the ensemble-mean SSH anomaly (only contours  $\geq 0.02$  m are shown) on every panel indicate the positive SSH anomaly of the downwelling Kelvin wave at this time. The different ensemble members differ in the phasing of the TIW field. Thus, the TIW and background flow components can be separated using an average over all 10 ensemble members.

phasing of the TIWs is different in each member (three example ensemble members are shown in Fig. 6 for the downwelling experiment). An average over the ensembles [the overbar in Eq. (6)] thus separates the TIW field while retaining the time and longitude dependence in both the TIW and background flow fields. The initialization times were distributed evenly over the last  $4 \times 34$  days of the control simulation as 34 days was the dominant TIW period.

Because of the computational expense of performing an ensemble of simulations, it was not possible to test more than one set of Kelvin wave parameters. We choose to examine intraseasonal Kelvin waves with a 60-day period, a dominant peak in the observed Kelvin wave spectrum (McPhaden and Taft 1988; Kessler et al. 1995; Cravatte et al. 2003). The amplitude of the forcing was tuned using a trial-and-error method to produce Kelvin waves with  $\pm 0.08$ -m variations in SSH,  $\pm 15$ -m variations in  $20^\circ\text{C}$  isotherm depth (Fig. 7a), and a maximum of  $\pm 1.5^\circ\text{C}$  variations in subsurface temperature at  $-140^\circ\text{E}$ . These values represent a strong but realistic Kelvin wave in comparison to observations (Johnson and McPhaden 1993a,b; Kessler et al. 1995; Cravatte et al. 2003; Jiang et al. 2009).

The propagation of the Kelvin waves across the basin is clearly visible in SSH and the  $20^\circ\text{C}$  isotherm depth (Figs. 7a–d). The ensemble average does a good job of removing the TIW variability (cf. Figs. 7a,b with Figs. 7c,d). The wave signal begins at  $-200^\circ\text{E}$  and is visible there over the forcing period of 30 days. The phase speed appears to be relatively constant across the basin, with only a small slowing from  $2.8 \text{ m s}^{-1}$  at  $-200^\circ\text{E}$  to  $2.68 \text{ m s}^{-1}$  at  $-140^\circ\text{E}$  predicted for an ideal Kelvin mode (see Fig. 5). The perturbations in the  $20^\circ\text{C}$  isotherm are largest in the eastern Pacific near  $-120^\circ\text{E}$  (Figs. 7c,d), where this isotherm approaches the surface (Fig. 2e). However, the signal in the  $20^\circ\text{C}$  isotherm is not visible east of  $-100^\circ\text{E}$  because this isotherm is restricted close to the surface there. Amplitude and phase speed changes in the far eastern Pacific east of  $-120^\circ\text{E}$  may be associated with the conversion of energy from the first baroclinic to the second baroclinic mode (Gill and King 1985; Cravatte et al. 2003). The forcing applied in the western Pacific also forces a westward-propagating Rossby wave signal visible in both SSH and  $20^\circ\text{C}$  isotherm depth (Fig. 7c,d, west of  $-200^\circ\text{E}$ ). In addition, there is evidence of Rossby waves reflected from the eastern boundary as a result of the incident Kelvin wave (not shown), which may have an additional impact on the TIWs at later

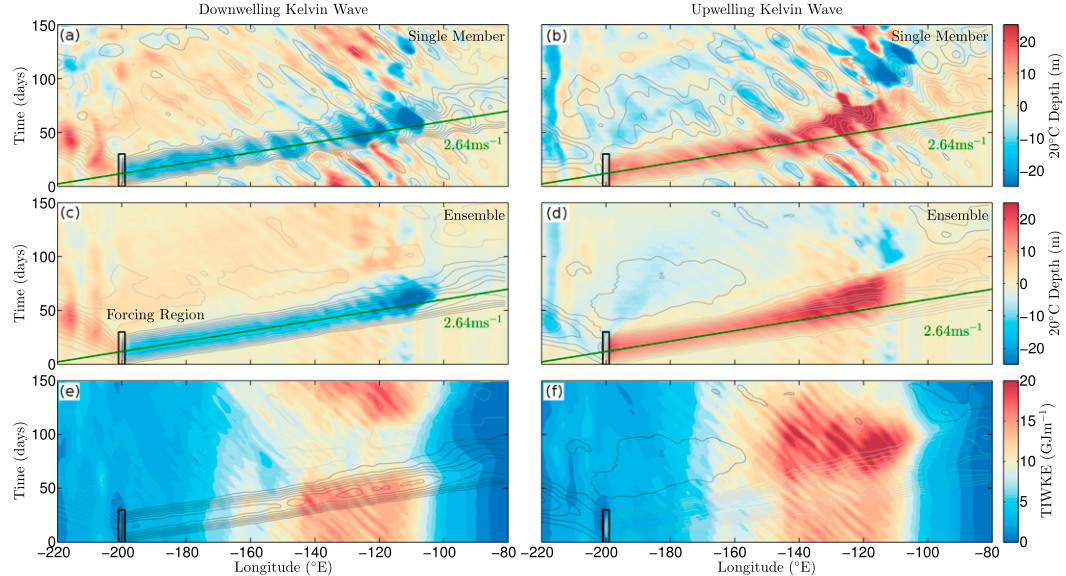


FIG. 7. Time-longitude plots of the 20°C isotherm depth anomaly on the equator for a single (a) downwelling and (b) upwelling ensemble member and for the ensemble average (c) downwelling and (d) upwelling experiments. Time-longitude plot of the TIWKE integrated over the top 244 m and between 7°S and 10°N for (e) downwelling and (f) upwelling experiments. Also shown are 0.01-m contours of SSH anomalies, with dark gray contours indicating positive values and light gray contours indicating negative values. The forcing region and time period is shown with a black box. The green line in (a)–(d) indicates a phase speed of  $2.64 \text{ m s}^{-1}$ .

times (Allen et al. 1995; Lawrence et al. 1998; Lawrence and Angell 2000; Benestad et al. 2001).

The Kelvin waves drive large variations in the latitude and depth-integrated TIWKE (Figs. 7e,f). TIWKE is suppressed by the downwelling wave and enhanced by the upwelling wave, in agreement with observations (Fig. 1; Qiao and Weisberg 1998). These changes occur uniformly with longitude in the region of TIW activity. The peak/trough in TIWKE occurs 20–30 days after the peak in the Kelvin wave pulse passes by. The TIWKE is then restored toward its original strength  $\sim 50$  days after the Kelvin wave has completely passed. There is some evidence of advection of TIWKE by the Kelvin wave in the far eastern Pacific (the colored contours between  $-100^\circ$  and  $-80^\circ\text{E}$  in Figs. 7e,f), but the large changes in TIWKE are clearly not due to Kelvin wave advection.

As discussed in the previous section, the TIWs gain energy from both the LSP and conversion of mean PE to TIWKE. The Kelvin waves alter the background zonal velocity  $U$  and density structure and thus may alter the balance of the TIWKE budget resulting in the growth and decay of TIWKE.

## 5. The modified TIWKE budget

We now examine the Kelvin wave-induced modifications to the TIWKE budget. First, the TIWKE budget

from the 10-member ensemble average at the initial time (not shown), well before the Kelvin wave arrives in the eastern Pacific, agrees well with the budget in the control simulation (Fig. 3). To describe how the budget is altered by the Kelvin waves, we examine time series of the TIWKE budget integrated over the control volume (as for Fig. 3) 7°S to 10°N,  $-150^\circ$  to  $-110^\circ\text{E}$  over the top 244 m (Figs. 8 and 9).

### a. Downwelling Kelvin wave

For the downwelling experiment, there is a small period of TIWKE growth followed by a decay of  $23.2 \pm 2.0 \text{ PJ}^2$  (or 38% of the control  $61.7 \pm 1.9 \text{ PJ}$ ) between days 43 and 77, beginning as the SSH signal of the Kelvin wave within the control volume peaks (cf. black line in Fig. 8b with the red line in Fig. 8a). Once the Kelvin wave has passed, the TIWKE is then restored to its control strength between day 99 and the end of the experiment. The small period of growth up to day 43 is partially driven by the convergent  $\partial U / \partial x < 0$  at the

<sup>2</sup>The estimated uncertainty of  $\pm 2.0 \text{ PJ}$  and all subsequent uncertainty estimates on volume- and time-integrated quantities from the ensemble experiments were calculated using the jackknife method (Efron and Stein 1981) as the  $\pm 2$  standard deviation ( $\sigma$ ) spread in the given quantity over 10 ensemble sets of nine members constructed by leaving one member out for each set.

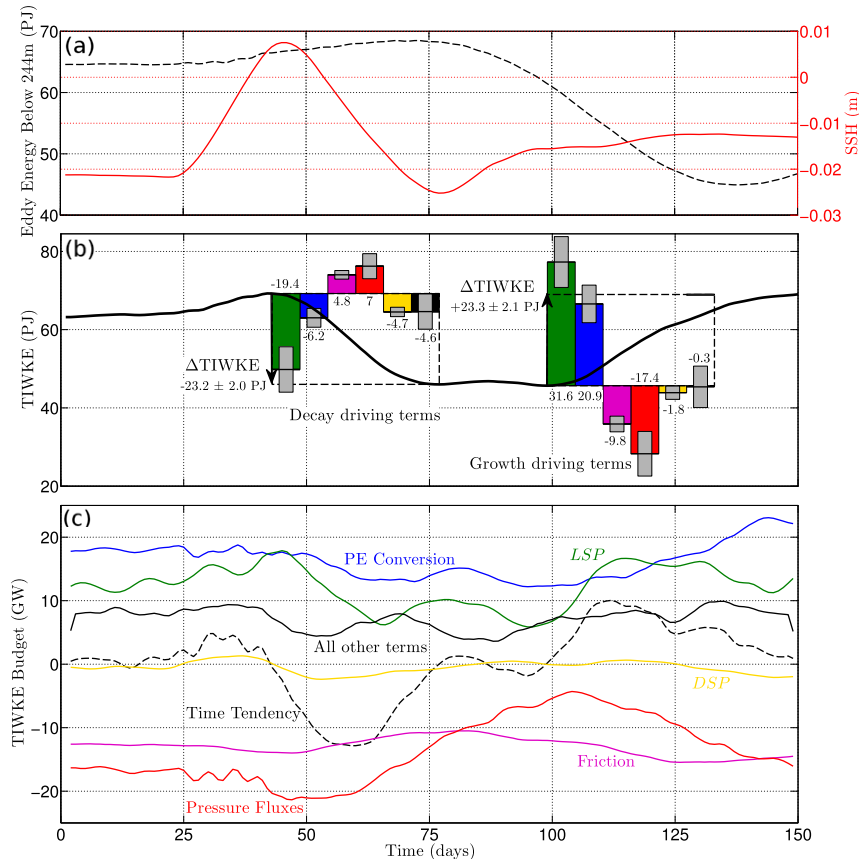


FIG. 8. TIWKE and TIWKE budget terms as a function of time integrated over the control volume bounded by latitudes 7°S and 10°N, longitudes -150° and -110°E, and above 244 m for the downwelling Kelvin wave experiment. (a) Eddy energy below 244 m (black dashed, left axis) and SSH (red, right axis). (b) TIWKE. (c) TIWKE budget terms including PE conversion (blue), LSP [Eq. (7); green], friction (purple), pressure flux divergence (red), time tendency (dashed black), DSP [Eq. (11); yellow], and all other terms included in the residual (solid black). In (b), each colored bar corresponds to the time integral of the corresponding colored term in (c) over the TIWKE decay (days 43 to 77) and growth (days 99 to 149) periods according to Eq. (12), indicating how much each term contributes to the net change in TIWKE (PJ) over these periods. The gray regions correspond to the  $\pm 2\sigma$  spread over 10 sets of nine ensemble members constructed using the jackknife method (see footnote 2).

leading edge of the downwelling Kelvin wave through the  $\partial U/\partial x$  shear production term

$$\text{DSP} = -\rho_0 \overline{u' u'} \frac{\partial U}{\partial x}, \quad (11)$$

(cf. yellow line and black dashed line in Fig. 8c). DSP shows a clear phase relationship with the Kelvin wave SSH field (cf. yellow line in Fig. 8c to red line in Fig. 8a) and a simple latitude-depth spatial structure similar to the Kelvin wave velocity field (not shown). The negative DSP associated with the divergent  $\partial U/\partial x > 0$  on the trailing edge of the Kelvin wave pulse also helps to initiate the decay in TIWKE after day 43 (yellow line in Fig. 8c soon

after day 43), along with the pressure flux radiation term (red line in Fig. 8c soon after day 43) and several other small terms in the budget (solid black line in Fig. 8c soon after day 43) including  $\partial V/\partial y$  production and mean advection (not shown). Once the decay in TIWKE is initiated, the LSP drops sharply, allowing a strong negative time tendency in TIWKE (cf. black dashed and green line in Fig. 8c between days 48 and 70). The subsequent growth in TIWKE after day 99 once the Kelvin wave has passed is also accompanied by a large change in LSP.

To establish which terms are responsible for the net changes in TIWKE, we time integrate the TIWKE budget over the decay (between days 43 and 77) and growth (between days 99 and 149) periods, subtracting off the

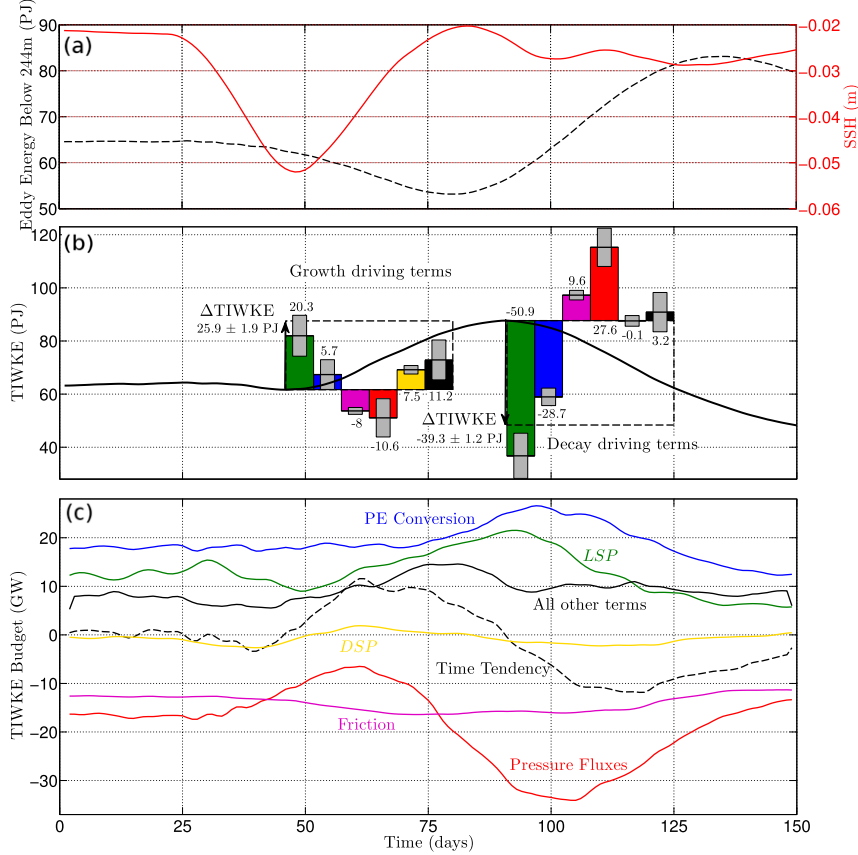


FIG. 9. As in Fig. 8, but for the upwelling Kelvin wave experiment. The TIWKE growth period in (b) is between days 46 and 91, and the decay period is between days 91 and 149.

initial budget. For example, the total contribution of changes in LSP to changes in volume-integrated TIWKE over a period between days  $t_1$  and  $t_2$  is

$$\int_{t_1}^{t_2} \int_V \text{LSP}(x, y, z, t) - \text{LSP}(x, y, z, t_1) dV dt, \quad (12)$$

where  $\int_V dV$  indicates an integral over the control volume, and the budget should be roughly balanced at time  $t_1$  to minimize the residual. Changes in LSP are the largest driver of changes in TIWKE, being responsible for  $19.4 \pm 5.8 \text{ PJ}$  of the reduction in TIWKE over the decay period and  $31.6 \pm 6.5 \text{ PJ}$  of the increase in TIWKE over the growth period (green bars in Fig. 8b). Other terms make small contributions, including the PE conversion (blue bars in Fig. 8b), DSP (yellow bars in Fig. 8b), and other terms (black bars in Fig. 8b). The frictional term generally opposes the changes in TIWKE with reduced (increased) friction during weak (strong) TIWKE periods (purple bars in Fig. 8b).

The rate at which energy is radiated out of the control volume via pressure fluxes changes as a

consequence of the changes in TIWKE (solid red line in Fig. 8c). Neither bottom drag or the loss of energy through radiation out of the lateral boundaries change significantly during the passage of the Kelvin wave (not shown), and thus the changes in pressure flux divergence are associated with changes in the transfer of energy between the upper (above 244 m) and deep (below 244 m) ocean. The reduction in TIWKE is followed by a decrease in the rate at which energy is radiated to depths below 244 m, which acts as a negative feedback on the TIWKE changes contributing  $7.0 \pm 3.2 \text{ PJ}$  of TIWKE during the decay period (first red bar in Fig. 8b). Subsequently, a decay of the eddy KE below 244 m occurs (black dashed line in Fig. 8a) where the variations in the eddy KE budget are dominated by a balance between time tendency and pressure flux divergence (not shown). Near the end of the time series the TIWKE at the surface is restored, followed by an increase in the downward radiation rate that begins to restore the eddy KE below 244 m (cf. red line in Fig. 8c with black dashed line in Fig. 8a after day 110).

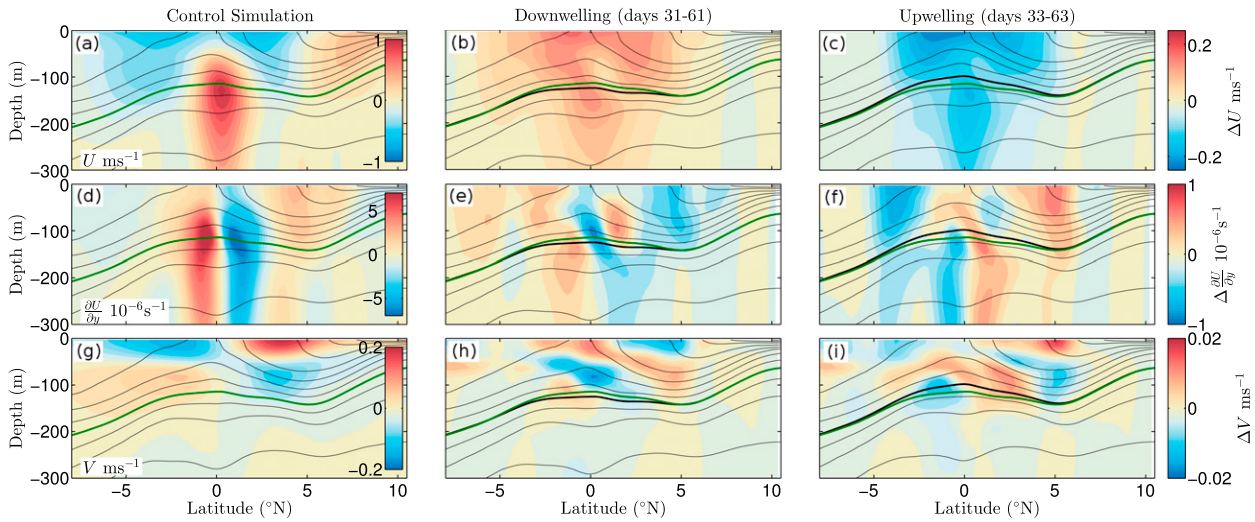


FIG. 10. (a) Zonal velocity  $U$ , (d)  $\partial U / \partial y$ , and (g) meridional velocity  $V$  from the control simulation ensemble and time averaged between the longitudes of  $-150^\circ$  and  $-110^\circ\text{E}$ . Deviations in these variables from the control simulation averaged over the (b),(e),(h) downwelling and (c),(f),(i) upwelling wave peaks between days 31–61 and 33–63, respectively. The contours indicate  $0.3 \text{ kg m}^{-3}$  isopycnals, and the  $1025.1 \text{ kg m}^{-3}$  isopycnal is highlighted using a thicker line. The green contour indicates the  $1025.1 \text{ kg m}^{-3}$  isopycnal from the control simulation on every panel. The downwelling (upwelling) wave results in a general weakening (strengthening) of the circulation except near the EUC core and below.

### b. Upwelling Kelvin wave

For the upwelling experiment, the TIWKE undergoes changes roughly the reverse of those occurring in the downwelling experiment. There is a short period of decay followed by a growth of  $25.9 \pm 1.9 \text{ PJ}$  (or 42% of the background  $61.7 \text{ PJ}$ ) between days 46 and 91, beginning as the peak SSH signal of the Kelvin wave passes through the control volume (cf. black line in Fig. 9b with red line in Fig. 9a). Once the Kelvin wave has passed by, the TIWKE then decays to values below its original strength by the end of the experiment. Once again, the LSP drives most of the changes in TIWKE (green bars in Fig. 9b). The DSP appears to play an important role in the initial weakening of TIWKE and then helps initiate the growth around day 50 (cf. black dashed and yellow lines in Fig. 9c). The rate at which TIWKE is radiated downward via pressure fluxes again acts as a negative feedback, driving an increase in the eddy KE below 244 m well after the increase in TIWKE at the surface (cf. red line in Fig. 9c with black dashed line in Fig. 9a).

### c. Changes in the background circulation

The growth and decay in TIWKE is a result of modifications to the background circulation by the Kelvin waves. The downwelling Kelvin wave alters the background flow by reducing the magnitude of the SEC and increasing the magnitude of the EUC by a smaller amount (cf. Figs. 10b and 10a). This differs from the structure of the Kelvin wave predicted using the

eigenvalue calculation described in the appendix that shows a stronger perturbation near the EUC core and weaker variations near the surface (Fig. 5f). The differences are due to other processes that are not taken into account in the eigenvalue calculation, such as wind forcing, nonlinearities, and the influence of the TIWs on the background circulation. For example, the enhanced relative amplitude near the surface may be due to alterations of the boundary layer depth  $H$  by the Kelvin wave pulses, which alter how wind-driven momentum penetrates the surface ocean. To estimate the potential influence of this process on the zonal velocity response, we assume that the frictional force within the boundary layer  $F_B$  is driven by a wind stress  $\tau$  such that  $F_B(H) = \tau/H/\rho_0$ . Equating an anomaly in this force to an anomalous acceleration  $\partial u / \partial t = \Delta u / \Delta t = F_B(H + \Delta H) - F_B(H)$  implies that variations in the boundary layer depth  $\Delta H$  can drive a velocity anomaly  $\Delta u$  of

$$\Delta u = -F_B(H) \frac{\Delta H}{H + \Delta H} \Delta t. \quad (13)$$

At  $-140^\circ\text{E}$ , the boundary layer depth reached 24 m (19 m) in the downwelling (upwelling) ensemble Kelvin wave experiments, and thus we estimate  $\Delta H = \pm 2.5 \text{ m}$ . We estimate  $F_B(H) = -4 \times 10^{-7} \text{ m s}^{-2}$  from an average of the control simulation model diagnostic zonal frictional force over the boundary layer depth of  $H = 21.5 \text{ m}$ . Using these values and the Kelvin wave pulse time scale of  $\Delta t = 30 \text{ days}$  results in velocity variations of

$\Delta u = \pm 0.12 \text{ m s}^{-1}$ . Thus, Kelvin wave–induced variations in the boundary layer depth could potentially explain some of the enhanced response in zonal velocity near the surface (cf. to velocity scale in Figs. 10b and 10c).

The net influence of the downwelling Kelvin wave is a weakening in the lateral shear  $\partial U/\partial y$  in most locations except near the EUC core and below (cf. Figs. 10e and 10d). In particular, the shear in regions between the SEC and NECC (near the surface near  $5^\circ\text{N}$  in Fig. 10e) and between the upper EUC and SEC (50-m depth near  $1^\circ\text{N}$  in Fig. 10e) weaken. In contrast, the upwelling wave results in a strengthened SEC (cf. Figs. 10c and 10a) and strengthened lateral shear in most regions except on either side of the EUC core and below (cf. Figs. 10f and 10d).

The Kelvin wave modifications to the buoyancy field appear to be relatively minor, with the only noticeable change occurring in the region near the EUC core (cf. thick green and thick black isopycnals in Figs. 10a–c). Changes also occur to the background meridional circulation, with the tropical cells weakening slightly in the downwelling experiment and strengthening in the upwelling experiment (cf. Figs. 10g–i). Overall, the downwelling Kelvin wave appears to drive a weakening of the background circulation consistent with the subsequent reduction in TIWKE. In contrast, the upwelling wave drives an overall strengthening of the circulation and thus an intensification of the TIWKE. However, the actual changes in the TIWKE budget presented above (Figs. 8 and 9) are complex, as we discuss in the next section.

#### d. The role of lateral shear production

The main net driver of the changes in TIWKE in the surface ocean is the LSP (green bars in Figs. 8b and 9b). However, the LSP depends on the TIWKE itself through the momentum flux  $u'v'$  [Eq. (7)], and thus much of the change in the LSP may be due to changes in the TIWKE itself, as opposed to changes in the background shear  $\partial U/\partial y$ . The relationship between the LSP and the TIWKE provides the system with its sensitive nature, where strong growth or decay in the TIWKE can be initiated by small changes to other terms in the TIWKE budget. The downwelling Kelvin wave causes a net negative perturbation to a number of terms in the TIWKE budget (as discussed in the previous section) that unbalances the TIWKE budget such that the net sink terms (friction and pressure flux radiation) dominate the source terms as the wave peak passes (day 43 in Fig. 8c). This results in a rapid decay in TIWKE that continues until the negative feedback associated with changes in the downward radiation of

energy via pressure fluxes reverses the trend by day 77 (red line in Fig. 8c). The situation is reversed for the upwelling wave.

To look at this process in more detail, we decompose the LSP term into its dependence on the TIWKE, the background shear, and the momentum flux normalized by the TIWKE:

$$\text{LSP}(x, y, z, t) = -\rho_0 \overline{u'v'} \frac{\partial U}{\partial y} = -\mathcal{K} C \frac{\partial U}{\partial y}, \quad (14)$$

where  $C = \overline{u'v'}/[0.5(\overline{u'u'} + \overline{v'v'})]$  is the normalized momentum flux. Now a further decomposition can be performed into terms involving the time-independent control simulation fields (denoted by superscript  $B$ ; see Fig. 3) and the varying fields (denoted by superscript  $D$ ):

$$\begin{aligned} \text{LSP}(x, y, z, t) = & \underbrace{-\mathcal{K}^B C^B \frac{\partial U^B}{\partial y}}_{\text{LSP}^{BBB}(x, y, z)} - \underbrace{\mathcal{K}^B C^B \frac{\partial U^D}{\partial y}}_{\text{LSP}^{BBD}(x, y, z, t)} \\ & - \underbrace{\mathcal{K}^B C^D \frac{\partial U^B}{\partial y}}_{\text{LSP}^{BDB}(x, y, z, t)} - \underbrace{\mathcal{K}^D C^B \frac{\partial U^B}{\partial y}}_{\text{LSP}^{DBB}(x, y, z, t)} \\ & + \underbrace{\text{Higher Order}}_{\text{LSP}^{\text{HO}}(x, y, z, t)}, \end{aligned} \quad (15)$$

where  $\text{LSP}^{BBB}$  denotes the shear production term from the control simulation, and  $\text{LSP}^{BBD}$  denotes the varying part associated with the varying component of the background shear  $(\partial U^D/\partial y)(x, y, z, t) = (\partial U/\partial y)(x, y, z, t) - (\partial U^B/\partial y)(x, y, z, t)$ . The  $\text{LSP}^{BDB}$  denotes the varying part associated with changes in the relationship between  $u'$  and  $v'$  through  $C$ ,  $\text{LSP}^{DBB}$  denotes the varying part associated with changes in the TIWKE  $\mathcal{K}$ , and  $\text{LSP}^{\text{HO}}$  denotes the remaining higher-order terms.

Time series of the terms in Eq. (15) for both downwelling (Fig. 11) and upwelling (Fig. 12) experiments show that the higher-order terms (yellow  $\text{LSP}^{\text{HO}}$  in Figs. 11b and 12b) are small relative to the other terms. The term associated with the varying background shear  $\text{LSP}^{BBD}$  shows a clear relationship with the Kelvin wave (cf. red dashed line in Figs. 11a and 12a with blue  $\text{LSP}^{BBD}$  in Figs. 11b and 12b). For the downwelling experiment, a negative perturbation in  $\text{LSP}^{BBD}$  peaks soon after the peak of the wave passes, consistent with an overall weakening of the background lateral shear  $\partial U/\partial y$  driven by the downwelling Kelvin wave (Fig. 10e). This supports the hypothesis of Qiao and Weisberg (1998) and conflicts with the suggestions of Harrison and Giese (1988) and Giese and Harrison (1991) that downwelling Kelvin waves increase TIWKE by increasing the magnitude of

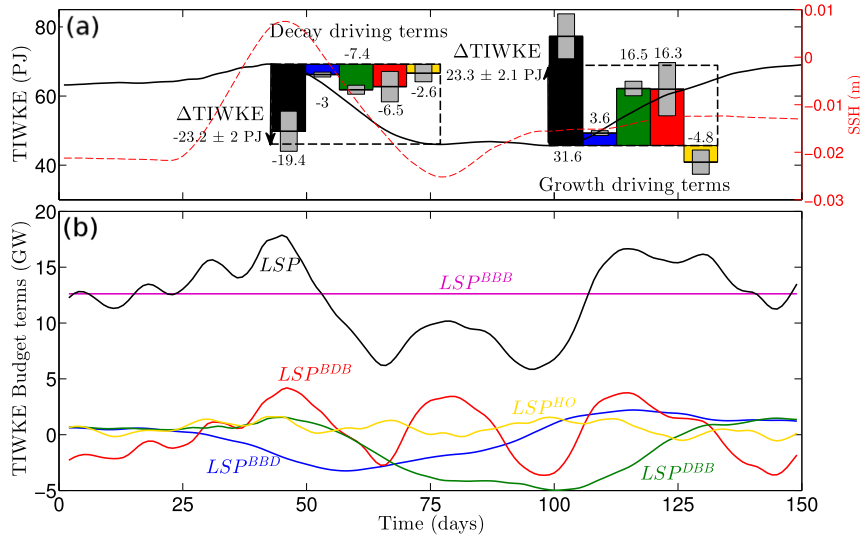


FIG. 11. (a) TIWKE (black line) and SSH (red dashed line) from the downwelling experiment as in Figs. 8a and 8b. (b) Component terms of the LSP (black line, identical to green line in Fig. 8c), according to Eq. (15).  $LSP^{BBB}$  denotes the value from the control simulation,  $LSP^{BDB}$  denotes the varying part associated with changes in the background shear  $\partial U/\partial y$ ,  $LSP^{DBD}$  denotes the varying part associated with changes in the correlation between  $u'$  and  $v'$ ,  $LSP^{DBB}$  denotes the varying part associated with changes in TIWKE, and  $LSP^{HO}$  denotes higher-order terms. The bars in (a) show the time-integrated contributions of each term in (b) calculated similarly to the bars in Fig. 8b.

$\partial U/\partial y$  on either side of the EUC. Our results suggest that this is not the case because the TIWKE (Fig. 3d) and momentum flux  $\bar{u}'\bar{v}'$  are weaker on either side of the EUC core and below (where the lateral shear is increased; Fig. 10e) than closer to the surface in the EUC–SEC and SEC–NECC shear regions (where the lateral shear is decreased; Fig. 10e).

While the changes in background shear through the  $LSP^{BBD}$  term do drive a decrease (increase) in TIWKE in the downwelling (upwelling) experiment, these changes are only a small proportion of the total TIWKE change driven by LSP (cf. blue and black bars in Figs. 11a and 12a). In both upwelling and downwelling experiments, the term associated with variations in the

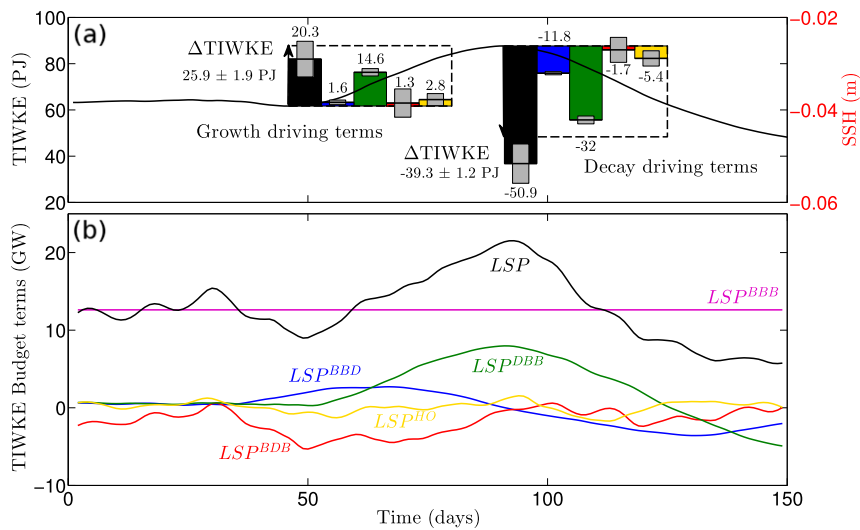


FIG. 12. As in Fig. 11, but for the upwelling experiment.

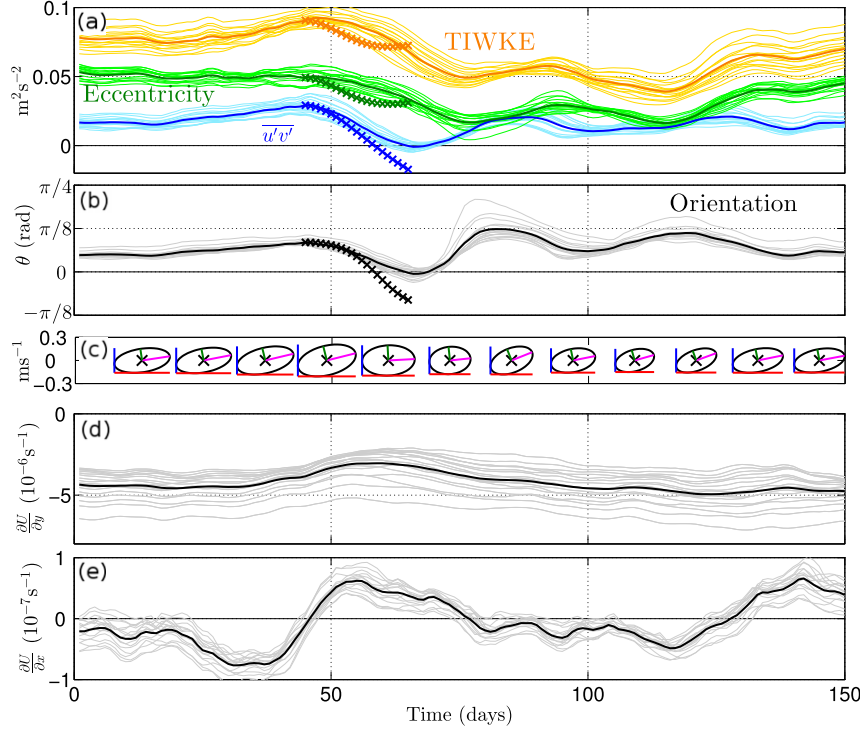


FIG. 13. (a) TIWKE, the momentum flux  $\overline{u'v'}$ , and ellipse eccentricity  $L = 0.5(\overline{u'u'} - \overline{v'v'})$  averaged between  $-150^\circ$  and  $-110^\circ\text{E}$  in the region  $1^\circ$  to  $1.75^\circ\text{N}$ , 92- to 63-m depth from the downwelling experiment. The thin lines denote each latitude-depth grid point within this region, and the thick lines denote their average. (c) TIW velocity covariance ellipses ( $\text{m s}^{-1}$ ) and their (b) orientation  $\theta$  corresponding to the momentum fluxes in (a). In (c), the magenta line is the major axis  $a$  [Eq. (16)] and the green line is the minor axis  $b$  [Eq. (17)]. Background (d)  $\partial U/\partial y$  and (e)  $\partial U/\partial x$  at the same locations as (a). The crosses in (a) and (b) show estimated changes in the corresponding properties driven by the changes in background shear in (d) and (e) between days 45 and 65 [see Eq. (19)].

TIWKE itself  $\text{LSP}^{DBB}$  is the largest contributor over both the decay and growth periods (green bars in Figs. 11a and 12a);  $\text{LSP}^{DBB}$  encapsulates the sensitive nature of the TIWKE budget. Any small initial perturbation in the TIWKE can be amplified by  $\text{LSP}^{DBB}$  as stronger (weaker) TIWs more (less) efficiently extract energy from the lateral shear of the background flow leading to a positive feedback.

Finally, variations in the correlation between  $u'$  and  $v'$ , through the term  $\text{LSP}^{DBB}$ , also play a role in driving variations in  $\text{LSP}$  (red line in Figs. 11b and 12b and red bars in Figs. 11a and 12a). In the downwelling experiment, the sharp drop in  $\text{LSP}^{DBB}$  between days 45 and 65 (contributing  $-6.5 \pm 4.4 \text{ PJ}$  to the drop in volume-integrated TIWKE; red bar in Fig. 11a) is mostly a consequence of changes in the EUC-SEC shear region near 80-m depth at  $1.5^\circ\text{N}$ . In this region,  $\overline{u'v'}$  drops almost to zero, despite much smaller changes in the TIWKE (cf. blue lines to brown lines in Fig. 13a). This can be understood by considering TIW eddy

covariance ellipses in this region, whose properties can be derived from the momentum fluxes

$$a^2 = \overline{u'u'} \cos^2 \theta + \overline{u'v'} \sin 2\theta + \overline{v'v'} \sin^2 \theta, \quad (16)$$

$$\begin{aligned} b^2 &= \overline{u'u'} \cos^2 \left( \theta + \frac{\pi}{2} \right) + \overline{u'v'} \sin 2 \left( \theta + \frac{\pi}{2} \right) \\ &\quad + \overline{v'v'} \sin^2 \left( \theta + \frac{\pi}{2} \right), \quad \text{and} \end{aligned} \quad (17)$$

$$\theta = 0.5 \tan^{-1} \left( \frac{\overline{u'v'}}{L} \right), \quad (18)$$

where  $a$  and  $b$  are the major and minor ellipse axis lengths,  $L = 0.5(\overline{u'u'} - \overline{v'v'})$  is the ellipse eccentricity, and  $\theta$  is the ellipse orientation (Waterman and Hoskins 2013). The covariance momentum flux  $\overline{u'v'}$  is only non-zero for eccentric  $L \neq 0$  ellipses oriented off the coordinate axes  $\theta \neq (n\pi)/2$ , where  $n$  is an integer. As for the TIWKE budget calculations above, the momentum fluxes are calculated from the ensemble deviation

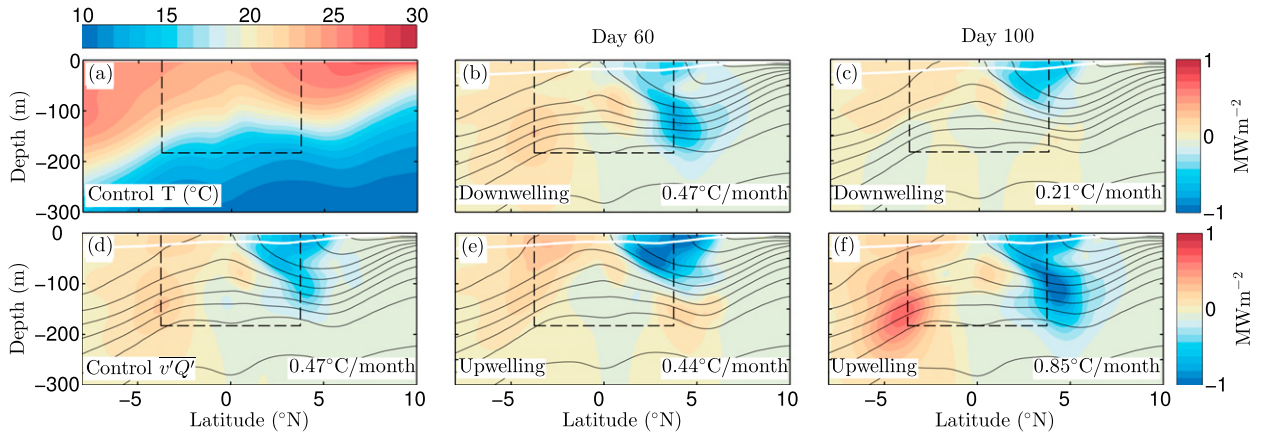


FIG. 14. (a) Temperature and (b)–(f) meridional eddy heat flux  $\bar{v}'\bar{Q}' = C_p\rho_0\bar{v}'\bar{T}'$ , where  $C_p$  is the specific heat and  $\rho_0$  is a reference density, averaged between  $-150^\circ$  and  $-110^\circ\text{E}$  from the control simulation in (a) and (d), on day 60 for the downwelling experiment in (b) and upwelling experiment in (e) and on day 100 for the downwelling experiment in (c) and upwelling experiment in (f). In the bottom-right corner of each panel, the average value of the induced heating ( $^\circ\text{C month}^{-1}$ ) over the control volume above  $-183\text{ m}$  and between  $\pm 3.75^\circ$  latitude (indicated with the dashed box) is shown. The white line indicates the boundary layer depth. On day 60, shortly following the Kelvin wave peak, the eddy fluxes are shifted vertically with no change in the magnitude of the heating they produce [(b) and (e)]. Later, on day 100, the eddy heat fluxes have reduced (increased) in the downwelling (upwelling) experiment due to the changes in TIWKE [(c) and (f)].

velocities at each location and then averaged between  $-150^\circ$  and  $-110^\circ\text{E}$ . Between days 45 and 65 the TIW eddy covariance ellipses (Fig. 13c) undergo a rotation such that the ellipse orientation  $\theta$  aligns closely with the zonal direction (Fig. 13b) and the eccentricity reduces (green lines in Fig. 13a), both of which result in a reduction in  $\bar{u}'\bar{v}'$  without necessarily changing the TIWKE [see Eq. (18)].

Kelvin wave–induced changes in the background shears  $\partial U/\partial y$  (Fig. 13d) and  $\partial U/\partial x$  (Fig. 13e) can potentially drive these changes in orientation and eccentricity through advective deformation of the TIW covariance ellipses. We consider the influence of these two shear components by examining evolution equations for the momentum fluxes:

$$\begin{aligned}\frac{\partial \bar{u}'\bar{u}'}{\partial t} &= -2\bar{u}'\bar{u}'\frac{\partial U}{\partial x} - 2\bar{u}'\bar{v}'\frac{\partial U}{\partial y} + \text{other terms}, \\ \frac{\partial \bar{u}'\bar{v}'}{\partial t} &= -\bar{v}'\bar{v}'\frac{\partial U}{\partial y} - \bar{u}'\bar{v}'\frac{\partial U}{\partial x} + \text{other terms},\end{aligned}\quad (19)$$

where we neglect the other terms such as friction, advection of the eddy flow by itself, and the Coriolis force. We also neglect changes driven by the shears in meridional velocity  $\partial V/\partial x$  and  $\partial V/\partial y$  (and thus the momentum flux  $\bar{v}'\bar{v}'$ ) as they are small at this location (Figs. 10g–i). Time evolving these equations beginning at time  $t_1 = 45$  using the measured initial momentum fluxes  $\bar{u}'\bar{v}'(t_i)$  and  $\bar{u}'\bar{u}'(t_i)$  and the measured deviation shears  $(\partial U/\partial y)(t) - (\partial U/\partial y)(t_i)$  and  $(\partial U/\partial x)(t) - (\partial U/\partial x)(t_i)$

gives a good prediction for the decay in  $\bar{u}'\bar{v}'$  (blue crosses in Fig. 13a). This reduction in  $\bar{u}'\bar{v}'$  is due not only to a reduction in the TIWKE (brown crosses in Fig. 13a) associated with LSP<sup>DDBB</sup>, but also because the Kelvin wave modifications in background shear reduce the eccentricity (green crosses in Fig. 13a) and rotate the ellipse orientation toward the east (black crosses in Fig. 13b), thus altering the phase relationship between  $u'$  and  $v'$  and driving a reduction in the LSP through LSP<sup>BDB</sup> in Eq. (15).

## 6. The equatorial heat budget

The growth and decay in TIWKE induced by the Kelvin waves results in changes in the TIW-driven meridional heat flux. The mean temperature balance is

$$\frac{\partial \bar{T}}{\partial t} = \bar{\mathcal{N}} - \nabla \cdot (\bar{\mathbf{u}} \bar{T} + \bar{\mathbf{u}}' \bar{T}'), \quad (20)$$

where  $\mathcal{N}$  represents nonconservative terms such as parameterized turbulent diffusion and penetrative solar radiation, and the other terms on the right-hand side are the convergence of mean and eddy fluxes. The overbar is defined as for the TIWKE budget (see section 3). In the control simulation, the TIWs transport heat southward across  $3.75^\circ\text{N}$  in the upper 200 m (Fig. 14d). There is also a weaker and deeper northward transport across  $3.75^\circ\text{S}$ . The net convergence of these fluxes acts to warm the upper equatorial region above 183 m by  $0.47^\circ\text{C month}^{-1}$ .

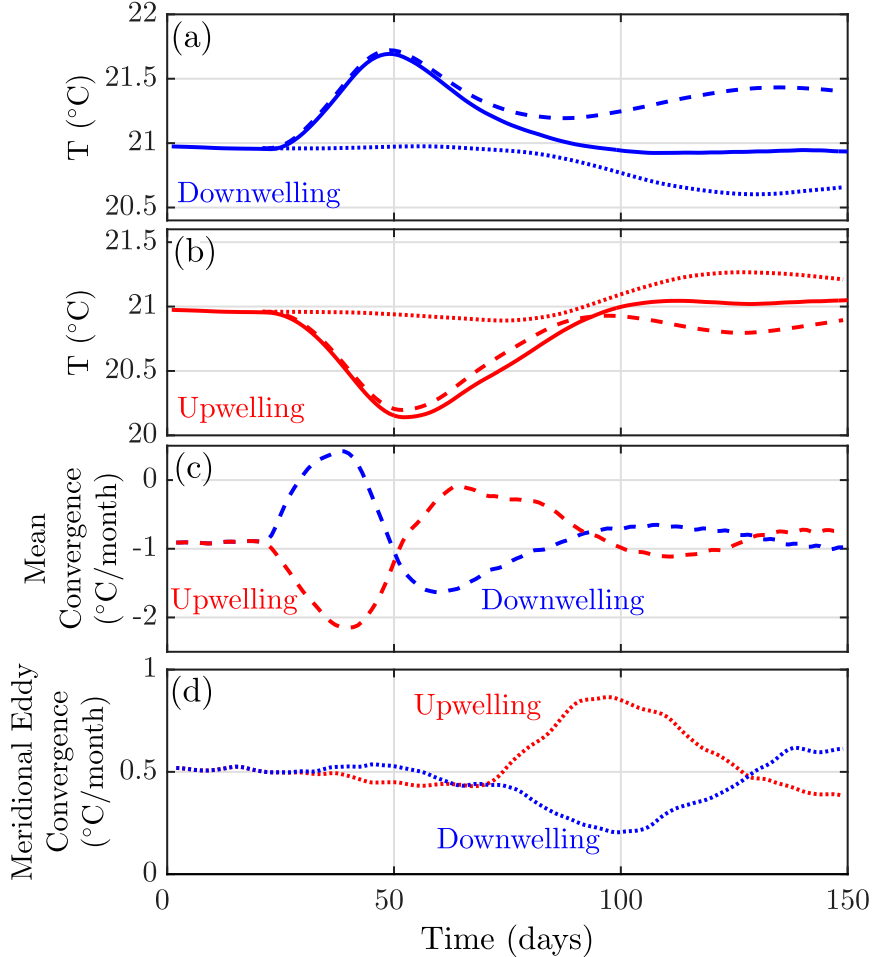


FIG. 15. Time series of terms in the heat budget (expressed in terms of an average temperature) of the upper equatorial ocean above  $-183\text{ m}$  between  $-150^\circ$  and  $-110^\circ\text{E}$ ,  $\pm 3.75^\circ$  latitude. Average temperature in (a) downwelling and (b) upwelling experiments (solid lines). (c) Convergence of mean heat fluxes  $-\nabla \cdot (\bar{\mathbf{u}} \bar{T})$  and (d) convergence of meridional eddy heat fluxes  $-\partial/\partial y(\bar{v} \bar{T})$  for both downwelling (blue) and upwelling (red) experiments. Also shown in (a) and (b) are the time-integrated mean convergence (dashed) and meridional eddy convergence (dotted) terms starting at day 21 just before the Kelvin waves arrive. The large initial changes in heat content are driven by the mean heat convergence through Kelvin wave zonal and vertical advection. Kelvin wave zonal advection drives a net change in heat content [cf. dashed lines in (a) and (b) before and after the Kelvin wave passes] that is compensated for by changes in the meridional eddy convergence [dotted lines in (a) and (b) after the Kelvin wave passes].

The Kelvin waves alter the TIW-driven meridional heat transport by modifying the background temperature gradients and the TIWKE. As the Kelvin waves pass, the meridional eddy heat flux patterns shift vertically without changing significantly in magnitude (Figs. 14b,e on day 60). Later (day 100), the meridional eddy heat fluxes are weakened in the downwelling experiment (meridional eddy heating reduces to  $0.21^\circ\text{C month}^{-1}$ ; Fig. 14c) and strengthened in the upwelling experiment (meridional eddy heating increases to  $0.85^\circ\text{C month}^{-1}$ ; Fig. 14f). These changes begin once

the TIWKE is maximally perturbed after day 75 and last until the TIWKE is restored to near its original values after day 125 (cf. Fig. 15d with Figs. 8b and 9b).

The changes in the meridional eddy heat fluxes play an important role in the heat budget of the upper equatorial ocean. The heat content of the upper equatorial ocean (expressed as an average temperature) in the control volume  $-150^\circ$  to  $-110^\circ\text{E}$ ,  $\pm 3.75^\circ$  latitude, upper  $183\text{ m}$ , undergoes a  $\sim 0.7^\circ\text{C}$  increase because of the downwelling Kelvin wave (solid line in Fig. 15a) and a  $\sim 0.7^\circ\text{C}$  decrease because of the upwelling Kelvin

wave (solid line in Fig. 15b). This is driven by zonal advection of the background zonal temperature gradient and vertical advection of the thermocline, which are both components of the mean heat convergence  $-\nabla \cdot (\bar{u} \bar{T})$  (Fig. 15c). The time integral of the mean heat convergence starting as the Kelvin waves arrive on day 21 describes the increase and subsequent decrease in heat content as the Kelvin wave peak passes through the control volume well (dashed lines in Figs. 15a and 15b). While the Kelvin wave-induced vertical advection is reversible, the zonal advection of a single Kelvin wave pulse is single signed and thus drives a net increase (decrease) in the heat content for the downwelling (upwelling) wave (as shown by the dashed lines in Figs. 15a and 15b that do not return to their initial values). However, this net change in heat content is counteracted by the changes in meridional eddy heat flux convergence (Fig. 15d) and time-integrated dotted lines in Figs. 15a and 15b), which restore the heat content to its initial value.

While the changes in the upper 200-m heat content are clear and coherent, the changes in SST and the mixed layer heat budget are more subtle (not shown). Mean zonal and vertical advection drive an initial SST warming (cooling) in the downwelling (upwelling) experiment of up to  $\pm 0.3^{\circ}\text{C}$ . There are also small changes in the diffusive term that reinforce the changes driven by mean advection. Following the passage of the Kelvin wave, both meridional and vertical eddy heating terms respond to the changes in TIWKE to drive SST cooling (warming) in the downwelling (upwelling) experiment. Thus, as for the upper 200-m heat content, the changes in TIW heat fluxes play an important role in compensating for the changes driven by the Kelvin wave and reducing the amplitude of the heat content and SST anomalies.

## 7. Summary and implications

Motivated by observations of the potential modulation of TIWs in the eastern equatorial Pacific by intraseasonal Kelvin waves (Fig. 1; Qiao and Weisberg 1998), we have examined the TIWKE budget in a set of  $1/4^{\circ}$  resolution ocean model simulations. In a control simulation with a statistically steady TIW field, the TIWKE budget is dominated by the creation of TIWKE through the release of PE and lateral shear production acting on the meridional shear in zonal velocity  $\partial U / \partial y$  (LSP) and the loss of TIWKE through friction and the radiation of waves (Fig. 3). Intraseasonal Kelvin waves propagating through the eastern Pacific change this budget by altering the background current shears and density structure that act as sources of energy for the

TIWs (Fig. 10). Strong downwelling Kelvin waves weaken the background circulation and can reduce the volume-integrated TIWKE by 38%. Upwelling Kelvin waves strengthen the background circulation and can intensify the volume-integrated TIWKE by 42%. The LSP is the main driver of the growth and decay of TIWKE (green lines in Figs. 8c and 9c), due mainly to a positive feedback associated with its dependence on the TIWKE itself (through the term  $\text{LSP}^{DBB}$  in Figs. 11b and 12b). However, the modifications to the TIWKE budget that initiate this growth and decay are complex, with a number of processes contributing. Among these are changes in the background shear  $\partial U / \partial y$  near the surface between the SEC and both the EUC and NECC ( $\text{LSP}^{BBB}$  in Figs. 11a and 12a) and zonal convergence/divergence of the zonal flow  $\partial U / \partial x$  on the leading and trailing edge of the Kelvin wave pulses (DSP in Figs. 8b and 9b). The changes in background shear also alter the correlation between  $u'$  and  $v'$  in the upper EUC, thus impacting the momentum flux  $\bar{u}'\bar{v}'$  independent of changes in the amplitude of the TIWs (Fig. 13).

In response to the modifications in TIWKE, the rate at which energy is radiated away from the TIW region via pressure fluxes also changes. Variations in the radiative loss of energy act as a negative feedback to stabilize the growth and decay of TIWKE (red lines in Figs. 8c and 9c). These changes are mostly associated with adjustments in the rate at which energy is radiated downward out of the surface ocean to the middepth and deep ocean below 244 m, with potential implications for the radiation of waves into the equatorial deep ocean, intraseasonal variability in the deep ocean, and abyssal mixing (Tanaka et al. 2015; Holmes et al. 2016).

Changes in TIWKE induced by propagating Kelvin waves have implications for SST variability in the eastern Pacific as TIWs play an important role in the mixed layer heat budget (Menkes et al. 2006; Jochum et al. 2007; Holmes and Thomas 2015). An initial investigation showed that the TIW-driven meridional heat flux undergoes significant changes in response to the changes in TIWKE, opposing the changes driven by mean advection and thus limiting the amplitude of the upper-ocean heat content anomaly associated with the Kelvin waves (Fig. 15). Changes in the mixed layer heat budget also showed evidence for eddy compensation that limits the amplitude of the SST anomaly (briefly discussed in section 6). However, these changes in the mixed layer heat budget were subtle and deserve to be studied further. One drawback of the current setup is that SST variability is damped by the assigned bulk flux forcing and fixed wind stress. Air-sea feedbacks

play an important role not only in allowing the upper ocean to adjust to perturbations in TIWKE and upper-ocean structure, but also by influencing the propagation of the Kelvin waves themselves (Hendon et al. 1998; Roundy and Kiladis 2006; Shinoda et al. 2008). How the interaction between Kelvin waves and TIWs influences the evolution of SST anomalies in the eastern equatorial Pacific remains an important question to be addressed by future research.

**Acknowledgments.** The computations were performed at the Stanford Center for Computational Earth and Environmental Science. We thank M. Jochum and S. Masina for helpful comments. R. Holmes was supported by a Robert and Marvel Kirby Stanford Graduate Fellowship while undertaking this study. The altimeter products (Fig. 1a) were produced and distributed by the Copernicus Marine and Environment Monitoring Service (CMEMS; <http://marine.copernicus.eu>). TMI data (Fig. 1b) are produced by Remote Sensing Systems and sponsored by the NASA Earth Sciences Program. Data are available at [www.remss.com](http://www.remss.com). This material is based upon work supported by the National Science Foundation under Grant 1260312 (LNT).

## APPENDIX

### Kelvin Wave Eigenfunction in a Zonally Uniform Background Flow

The derivation here is similar to that in McPhaden et al. (1986) except that the background buoyancy field is not assumed to be in geostrophic balance with the zonal velocity. We start with the hydrostatic, traditional equations of motion linearized about a zonally uniform background flow with zonal velocity  $U(y, z)$  and buoyancy field  $B(y, z)$  into which we substitute an assumed wave form in the zonal direction and time  $\{u, v, w, b, \phi\}(y, z)e^{i(kx - \omega t)}$ :

$$\begin{aligned} -ik(c - U)u + vU_y + wU_z - fv &= -ik\phi, \\ fu &= -\phi_y, \\ -b &= -\phi_z, \\ iku + v_y + w_z &= 0, \text{ and} \\ -ik(c - U)b + vB_y + wN^2 &= 0, \end{aligned}$$

where the subscripts denote differentiation,  $N^2 = B_z$ ,  $c = \omega/k$ , and  $f = \beta y$ , and we have made the longwave

approximation. These equations can be combined into a single equation for the pressure perturbation  $\phi$ :

$$\begin{aligned} A\phi_{yy} + B\phi_{yz} + C\phi_{zz} + D\phi_y + E\phi_z \\ - \frac{1}{c - U}(F\phi_z + G\phi) = 0, \end{aligned} \quad (\text{A1})$$

where,

$$A = 1, \quad (\text{A2})$$

$$B = \frac{1}{N^2}(fU_z - B_y), \quad (\text{A3})$$

$$C = \frac{f}{N^2}(f - U_y), \quad (\text{A4})$$

$$D = -\frac{2}{y} - \frac{S_y}{S} - \frac{B_{yz}}{N^2} - B_y \left( \frac{1}{N^2} \right)_z + \frac{B_y S_z}{N^2 S}, \quad (\text{A5})$$

$$\begin{aligned} E = f \left( \frac{U_z}{N^2} \right)_y + \frac{U_z f}{N^2} \left( \frac{B_y S_z}{N^2 S} - \frac{1}{y} - \frac{S_y}{S} - \frac{B_{yz}}{N^2} \right) \\ + \left( f^2 S - \frac{2fU_z B_y}{N^2} \right) \left( \frac{1}{N^2} \right)_z - \frac{fB_y U_{zz}}{N^4}, \end{aligned} \quad (\text{A6})$$

$$F = \frac{f}{N^2}(fU_z + B_y), \quad (\text{A7})$$

$$G = \beta + \frac{fS_y}{S} + \frac{fB_{yz}}{N^2} + fB_y \left( \frac{1}{N^2} \right)_z - \frac{fB_y S_z}{N^2 S}, \text{ and} \quad (\text{A8})$$

$$S = 1 - \frac{U_y}{f} + \frac{B_y U_z}{N^2 f}. \quad (\text{A9})$$

Equation (A1) becomes identical to Eq. (4) of McPhaden et al. (1986) when assuming that the background flow is in thermal wind balance  $B_y = -fU_z$ . Once  $\phi$  is obtained, the other variables can be obtained through the polarization relations:

$$u = -\frac{1}{f}\phi_y, \quad (\text{A10})$$

$$b = \phi_z, \quad (\text{A11})$$

$$w = \frac{ik}{N^2}(c - U)\phi_z - v\frac{B_y}{N^2}, \text{ and} \quad (\text{A12})$$

$$v = \frac{ik}{fS} \left[ \phi + \frac{U_z}{N^2}(c - U)\phi_z - (c - U)u \right]. \quad (\text{A13})$$

Equation (A1) is solved using MATLAB'S *eigs* routine (where  $c$  is the eigenvalue) using second-order finite differences. The boundary conditions used on  $\phi$  are that  $\partial\phi/\partial z = 0$  at  $z = 0, -H$  and  $\phi = 0$  at  $y = \pm L$ , where  $L$  is taken as  $15^\circ$  latitude.

To ensure that the first baroclinic mode Kelvin wave is correctly identified, a number of solutions are

obtained at different values of the parameter  $\alpha$  between 0 and 1, where the background flow  $U$  and  $B$  above are given by

$$U = \alpha U_R, \quad (A14)$$

$$B = \frac{1}{2L} \int_{-L}^L B_R dy + \alpha \left( B_R - \frac{1}{2L} \int_{-L}^L B_R dy \right),$$

where  $U_R$  and  $B_R$  are the zonal velocity and buoyancy fields averaged over the control simulation and over the forcing longitudes between  $-201^\circ$  and  $-199^\circ\text{E}$ . For  $\alpha = 0$ , there is no background flow, and the background buoyancy field is meridionally uniform. In this case, standard zero-mean flow wave theory gives wave modes that are separable into baroclinic (stretched cosines/sines under the WKB approximation) and meridional modes (cylindrical functions). As the mean flow is introduced by increasing  $\alpha$  from 0 toward 1, the first baroclinic mode Kelvin wave acquires significant small-scale structure (Figs. 5a–c). However, the large-scale structure remains similar, and the mode is easily identified among the other modes with large wave speeds (not shown).

## REFERENCES

- Allen, M. R., S. P. Lawrence, M. J. Murray, C. T. Mutlow, T. N. Stockdale, D. T. Llewellyn-Jones, and D. L. T. Anderson, 1995: Control of tropical instability waves in the Pacific. *Geophys. Res. Lett.*, **22**, 2581–2584, doi:10.1029/95GL02653.
- An, S., 2008: Interannual variations of the tropical ocean instability wave and ENSO. *J. Climate*, **21**, 3680–3686, doi:10.1175/2008JCLI1701.1.
- Benestad, R. E., R. T. Sutton, M. R. Allen, and D. L. T. Anderson, 2001: The influence of subseasonal wind variability on tropical instability waves in the Pacific. *Geophys. Res. Lett.*, **28**, 2041–2044, doi:10.1029/2000GL012563.
- Bergman, J. W., H. H. Hendon, and K. M. Weickmann, 2001: Intraseasonal air-sea interactions at the onset of El Niño. *J. Climate*, **14**, 1702–1719, doi:10.1175/1520-0442(2001)014<1702:IASIAT>2.0.CO;2.
- Contreras, R. F., 2002: Long-term observations of tropical instability waves. *J. Phys. Oceanogr.*, **32**, 2715–2722, doi:10.1175/1520-0485-32.9.2715.
- Cox, M. D., 1980: Generation and propagation of 30-day waves in a numerical model of the Pacific. *J. Phys. Oceanogr.*, **10**, 1168–1186, doi:10.1175/1520-0485(1980)010<1168:GAPODW>2.0.CO;2.
- Cravatte, S., J. Picaut, and G. Eldin, 2003: Second and first baroclinic Kelvin modes in the equatorial Pacific at intraseasonal timescales. *J. Geophys. Res.*, **108**, 3266, doi:10.1029/2002JC001511.
- Efron, B., and C. Stein, 1981: The jackknife estimate of variance. *Ann. Stat.*, **9**, 586–596, doi:10.1214/aos/1176345462.
- Farrar, J. T., 2011: Barotropic Rossby waves radiating from tropical instability waves in the Pacific Ocean. *J. Phys. Oceanogr.*, **41**, 1160–1181, doi:10.1175/2011JPO4547.1.
- Flament, P., S. Kennan, R. Knox, P. Niiler, and R. Bernstein, 1996: The three-dimensional structure of an upper ocean vortex in the tropical Pacific Ocean. *Nature*, **383**, 610–613, doi:10.1038/383610a0.
- Giese, B. S., and D. E. Harrison, 1990: Aspects of the Kelvin wave response to episodic wind forcing. *J. Geophys. Res.*, **95**, 7289–7312, doi:10.1029/JC095iC05p07289.
- , and —, 1991: Eastern equatorial Pacific response to three composite westerly wind types. *J. Geophys. Res.*, **96**, 3239–3248, doi:10.1029/90JC01861.
- Gill, A., and B. King, 1985: The effect of a shoaling thermocline on equatorially-trapped Kelvin waves. Meteorological Office Dynamical Climatology Tech. Note Met O 20, 36 pp.
- Graham, T., 2014: The importance of eddy permitting model resolution for simulation of the heat budget of tropical instability waves. *Ocean Modell.*, **79**, 21–32, doi:10.1016/j.ocemod.2014.04.005.
- Harrison, D. E., and B. S. Giese, 1988: Remote westerly wind forcing of the eastern equatorial Pacific; some model results. *Geophys. Res. Lett.*, **15**, 804–807, doi:10.1029/GL015i008p00804.
- Hendon, H. H., B. Liebmann, and J. D. Glick, 1998: Oceanic Kelvin waves and the Madden-Julian oscillation. *J. Atmos. Sci.*, **55**, 88–101, doi:10.1175/1520-0469(1998)055<0088:OKWATM>2.0.CO;2.
- Holmes, R. M., and L. N. Thomas, 2015: The modulation of equatorial turbulence by tropical instability waves in a regional ocean model. *J. Phys. Oceanogr.*, **45**, 1155–1173, doi:10.1175/JPO-D-14-0209.1.
- , —, L. Thompson, and D. Darr, 2014: Potential vorticity dynamics of tropical instability vortices. *J. Phys. Oceanogr.*, **44**, 995–1011, doi:10.1175/JPO-D-13-0157.1.
- , J. N. Moum, and L. N. Thomas, 2016: Evidence for seafloor-intensified mixing by surface-generated equatorial waves. *Geophys. Res. Lett.*, **43**, 1202–1210, doi:10.1002/2015GL066472.
- Jiang, C. L., L. A. Thompson, K. A. Kelly, and M. F. Cronin, 2009: The roles of intraseasonal Kelvin waves and tropical instability waves in SST variability along the equatorial Pacific in an isopycnal ocean model. *J. Climate*, **22**, 3470–3487, doi:10.1175/2009JCLI2767.1.
- Jochum, M., M. Cronin, W. Kessler, and D. Shea, 2007: Observed horizontal temperature advection by tropical instability waves. *Geophys. Res. Lett.*, **34**, L09604, doi:10.1029/2007GL029416.
- Johnson, E. S., and M. J. McPhaden, 1993a: Effects of a three-dimensional mean flow on intraseasonal Kelvin waves in the equatorial Pacific Ocean. *J. Geophys. Res.*, **98**, 10 185–10 194, doi:10.1029/93JC00759.
- , and —, 1993b: Structure of intraseasonal Kelvin waves in the equatorial Pacific Ocean. *J. Phys. Oceanogr.*, **23**, 608–625, doi:10.1175/1520-0485(1993)023<0608:SOIKWI>2.0.CO;2.
- Kennan, S., and P. Flament, 2000: Observations of a tropical instability vortex. *J. Phys. Oceanogr.*, **30**, 2277–2301, doi:10.1175/1520-0485(2000)030<2277:OOAVT>2.0.CO;2.
- Kessler, W. S., M. J. McPhaden, and K. M. Weickmann, 1995: Forcing of intraseasonal Kelvin waves in the equatorial Pacific. *J. Geophys. Res.*, **100**, 10 613–10 631, doi:10.1029/95JC00382.
- Large, W. G., and S. Yeager, 2004: Diurnal to decadal global forcing for ocean and sea-ice models: The data sets and flux climatologies. NCAR Tech. Note NCAR/TN-460+STR, 112 pp., doi:10.5065/D6KK98Q6.
- , J. C. McWilliams, and S. C. Doney, 1994: Oceanic vertical mixing: A review and a model with a nonlocal boundary layer

- parameterization. *Rev. Geophys.*, **32**, 363–403, doi:10.1029/94RG01872.
- Lawrence, S., and J. Angell, 2000: Evidence for Rossby wave control of tropical instability waves in the Pacific Ocean. *Geophys. Res. Lett.*, **27**, 2257–2260, doi:10.1029/1999GL002363.
- , M. R. Allen, D. L. T. Anderson, and D. T. Llewellyn-Jones, 1998: Effects of subsurface ocean dynamics on instability waves in the tropical Pacific. *J. Geophys. Res.*, **103**, 18 649–18 663, doi:10.1029/98JC01684.
- Legeckis, R., 1977: Long waves in the eastern equatorial Pacific Ocean: A view from a geostationary satellite. *Science*, **197**, 1179–1181, doi:10.1126/science.197.4309.1179.
- Lien, R.-C., D. R. Caldwell, M. C. Gregg, and J. N. Moum, 1995: Turbulence variability at the equator in the central Pacific at the beginning of the 1991–1993 El Niño. *J. Geophys. Res.*, **100**, 6881–6898, doi:10.1029/94JC03312.
- Luther, D. S., and E. S. Johnson, 1990: Eddy energetics in the upper equatorial Pacific during the Hawaii-to-Tahiti shuttle experiment. *J. Phys. Oceanogr.*, **20**, 913–944, doi:10.1175/1520-0485(1990)020<0913:EEITUE>2.0.CO;2.
- Lyman, J. B., G. Johnson, and W. Kessler, 2007: Distinct 17- and 33-day tropical instability waves in subsurface observations. *J. Phys. Oceanogr.*, **37**, 855–872, doi:10.1175/JPO3023.1.
- Malardé, J.-P., C. Perigaud, P. De Mey, and J.-F. Minster, 1987: Observation of long equatorial waves in the Pacific Ocean by Seasat altimetry. *J. Phys. Oceanogr.*, **17**, 2273–2279, doi:10.1175/1520-0485(1987)017<2273:OLEWI>2.0.CO;2.
- Marchesiello, P., X. Capet, C. Menkes, and S. Kennan, 2011: Submesoscale dynamics in tropical instability waves. *Ocean Model.*, **39**, 31–46, doi:10.1016/j.ocemod.2011.04.011.
- Masina, S., S. Philander, and A. Bush, 1999: An analysis of tropical instability waves in a numerical model of the Pacific Ocean: 2. Generation and energetics of the waves. *J. Geophys. Res.*, **104**, 29 637–29 661, doi:10.1029/1999JC00226.
- McPhaden, M. J., 2002: Mixed layer temperature balance on intraseasonal timescales in the equatorial Pacific Ocean. *J. Climate*, **15**, 2632–2647, doi:10.1175/1520-0442(2002)015<2632:MLTBOI>2.0.CO;2.
- , and B. A. Taft, 1988: Dynamics of seasonal and intra-seasonal variability in the eastern equatorial Pacific. *J. Phys. Oceanogr.*, **18**, 1713–1732, doi:10.1175/1520-0485(1988)018<1713:DOSAIV>2.0.CO;2.
- , J. A. Proehl, and L. M. Rothstein, 1986: The interaction of equatorial Kelvin waves with realistically sheared zonal currents. *J. Phys. Oceanogr.*, **16**, 1499–1515, doi:10.1175/1520-0485(1986)016<1499:TIOEKW>2.0.CO;2.
- Menkes, C., J. Vialard, S. Kennan, J. Boulanger, and G. Madec, 2006: A modeling study of the impact of tropical instability waves on the heat budget of the eastern equatorial Pacific. *J. Phys. Oceanogr.*, **36**, 847–865, doi:10.1175/JPO2904.1.
- Moum, J., R.-C. Lien, A. Perlin, J. Nash, M. Gregg, and P. Wiles, 2009: Sea surface cooling at the equator by subsurface mixing in tropical instability waves. *Nat. Geosci.*, **2**, 761–765, doi:10.1038/ngeo657.
- Pezzi, L. P., and K. J. Richards, 2003: Effects of lateral mixing on the mean state and eddy activity of an equatorial ocean. *J. Geophys. Res.*, **108**, 3371, doi:10.1029/2003JC001834.
- Philander, S., 1976: Instabilities of zonal equatorial currents. *J. Geophys. Res.*, **81**, 3725–3735, doi:10.1029/JC081i021p03725.
- Picaut, J., F. Masia, and Y. du Penhoat, 1997: An advective-reflective conceptual model for the oscillatory nature of the ENSO. *Science*, **277**, 663–666, doi:10.1126/science.277.5326.663.
- Qiao, L., and R. H. Weisberg, 1995: Tropical instability wave kinematics: Observations from the tropical instability wave experiment. *J. Geophys. Res.*, **100**, 8677–8693, doi:10.1029/95JC00305.
- , and —, 1998: Tropical instability wave energetics: Observations from the tropical instability wave experiment. *J. Phys. Oceanogr.*, **28**, 345–360, doi:10.1175/1520-0485(1998)028<0345:TIWEOF>2.0.CO;2.
- Roundy, P. E., and G. N. Kiladis, 2006: Observed relationships between oceanic Kelvin waves and atmospheric forcing. *J. Climate*, **19**, 5253–5272, doi:10.1175/JCLI3893.1.
- Shchepetkin, A., and J. McWilliams, 2005: The Regional Oceanic Modeling System (ROMS): A split-explicit, free-surface, topography-following-coordinate oceanic model. *Ocean Modell.*, **9**, 347–404, doi:10.1016/j.ocemod.2004.08.002.
- Shinoda, T., P. E. Roundy, and G. N. Kiladis, 2008: Variability of intraseasonal Kelvin waves in the equatorial Pacific Ocean. *J. Phys. Oceanogr.*, **38**, 921–944, doi:10.1175/2007JPO3815.1.
- Suarez, M. J., and P. S. Schopf, 1988: A delayed action oscillator for ENSO. *J. Atmos. Sci.*, **45**, 3283–3287, doi:10.1175/1520-0469(1988)045<3283:ADAOFE>2.0.CO;2.
- Tanaka, Y., T. Hibiya, and H. Sasaki, 2015: Downward lee wave radiation from tropical instability waves in the central equatorial Pacific Ocean: A possible energy pathway to turbulent mixing. *J. Geophys. Res.*, **120**, 7137–7149, doi:10.1002/2015JC011017.
- Wang, C., and P. C. Fiedler, 2006: ENSO variability and the eastern tropical Pacific: A review. *Prog. Oceanogr.*, **69**, 239–266, doi:10.1016/j.pocean.2006.03.004.
- Waterman, S., and B. J. Hoskins, 2013: Eddy shape, orientation, propagation, and mean flow feedback in western boundary current jets. *J. Phys. Oceanogr.*, **43**, 1666–1690, doi:10.1175/JPO-D-12-0152.1.
- Wentz, F., C. Gentemann, and K. Hilburn, 2015: Remote sensing systems TRMM TMI 3-day environmental suite on 0.25 deg grid, version 7.1. Remote Sensing Systems, accessed 12 January 2015. [Available online at [www.remss.com/missions/tmi](http://www.remss.com/missions/tmi).]
- Willett, C. S., R. R. Leben, and M. F. Lavn, 2006: Eddies and tropical instability waves in the eastern tropical Pacific: A review. *Prog. Oceanogr.*, **69**, 218–238, doi:10.1016/j.pocean.2006.03.010.
- Zhang, C., 2001: Intraseasonal perturbations in sea surface temperatures of the equatorial eastern Pacific and their association with the Madden-Julian oscillation. *J. Climate*, **14**, 1309–1322, doi:10.1175/1520-0442(2001)014<1309:IPISST>2.0.CO;2.